



HAL
open science

Bearing damage identification in oxide/oxide ceramic matrix composite with a new test design

Marion Broutelle, Frederic Lachaud, Ludovic Barriere, Alain Daidié,
Alexandre Chardonneau, Florent Bouillon

► **To cite this version:**

Marion Broutelle, Frederic Lachaud, Ludovic Barriere, Alain Daidié, Alexandre Chardonneau, et al.. Bearing damage identification in oxide/oxide ceramic matrix composite with a new test design. Composite Structures, 2020, 236, pp.111902 1-17. 10.1016/j.compstruct.2020.111902 . hal-02462012

HAL Id: hal-02462012

<https://hal.science/hal-02462012>

Submitted on 21 Jul 2022

HAL is a multi-disciplinary open access archive for the deposit and dissemination of scientific research documents, whether they are published or not. The documents may come from teaching and research institutions in France or abroad, or from public or private research centers.

L'archive ouverte pluridisciplinaire **HAL**, est destinée au dépôt et à la diffusion de documents scientifiques de niveau recherche, publiés ou non, émanant des établissements d'enseignement et de recherche français ou étrangers, des laboratoires publics ou privés.



Distributed under a Creative Commons Attribution - NonCommercial 4.0 International License

Bearing damage identification in oxide/oxide ceramic matrix composite with a new test design

Marion Broutelle ^{1,2}, Frédéric Lachaud ^{1*}, Ludovic Barrière ², Alain Daidié ¹, Alexandre Chardonneau ¹, Florent Bouillon ³

¹ Institut Clément Ader (ICA), Université de Toulouse, ISAE-SUPAERO, INSA, IMT MINES ALBI, UTIII, CNRS
3 Rue Caroline Aigle, 31400 Toulouse, France

² IRT Saint-Exupéry
118 route de Narbonne – CS44248, 31432 Toulouse Cedex 4, France

³ SAFRAN Ceramics
Rue de Touban, Les Cinq Chemins, 33185 Le Haillan, France

*To whom correspondence should be addressed: Tel. +33561338568, E-mail: frederic.lachaud@isae-supero.fr

Abstract

In this paper, the mechanisms of damage of an oxide/oxide ceramic matrix composite bearing are studied with a new experimental setup, the balanced quarter hole device (BQH). This test was designed to allow direct observation of the damage development on a material subjected to bearing failure. In a standard bearing experiment, real time monitoring is extremely difficult to set up, and post mortem observations of the bearing plane can be biased by the cutting operation. High speed cameras were used to take pictures of the bearing plane so that the damage development could be studied and a damage chronology established. The validity of the setup was verified by comparing the results obtained with those of a standard bearing test. Two different stacking sequences were studied, and the influence of the material microstructure and composite machining was investigated. It was shown that the first critical damage, matrix cracks, appeared before the load drop, and then led to delamination and kink bands, causing the final failure of the material.

Keywords

Ceramic matrix composite, damage mechanisms, bearing failure

Introduction

Due to current economic and environmental requirements, new materials are being introduced in aeronautical structures. Thanks to their low density and their mechanical properties at high temperatures, ceramic matrix composites (CMC) are considered to be good candidates for thermostructural applications. At intermediate temperatures (700 - 800 °C), oxide/oxide CMC are particularly interesting compared to carbide based CMC. They do not suffer from oxidation issues, and their manufacturing process is less expensive and faster [1].

The mechanical behavior of oxide/oxide CMC relies on the concept of a weak matrix [2]. This concept is allowed by partial sintering during the manufacturing of the composite. The porosity rate and size must be carefully controlled in order to obtain a material with interesting properties [3, 4] as the use of a highly porous matrix allows crack deflection at the fiber/matrix interface, resulting in fiber/matrix debonding and fiber pull out [5, 6]. When a crack develops in the porous matrix, it does not break the

fiber instantly and the composite lifetime is thus extended. Although the fibers and matrix are fragile, the composite shows damage tolerant behavior [1, 3].

If oxide/oxide CMC are to be used in hot sections of aircraft engines, it is necessary to study the damage and rupture occurring when the material is linked with the rest of the structure. In bolted joints, several types of failure can appear [7], depending, for instance, on the geometry or the stacking sequence of the specimen [8, 9]. There are three main types of failures (net tension, shearing and bearing) to which must be added the mixed modes and bolt failures. This study focuses on the bearing failure, which is a progressive, non-catastrophic degradation during which load transfer remains possible even after the appearance of the first damage [10].

Some studies have focused on the compressive behavior of similar materials. According to Ben Ramdane et al. [11], matrix cracks are initiated by macropores induced by the manufacturing process, and propagate along the fibers, creating delamination in the composite. Delamination is the main damage in the structure and leads to the final failure. Jackson et al. [12] pointed out that, in compression, the behavior is nearly linear until failure and that the structure fails suddenly just after the first damage (the buckling of the 0° plies).

To the best of our knowledge, there is no reference in the literature for the bearing capacities of oxide/oxide CMC but several authors have studied the damage chronology for similar materials, such as organic matrix composite. Bearing failure is due to an accumulation of several damage events in the structure [10]. This damage consists of fiber micro-buckling leading to kinking, matrix breakage, delamination and shear bands through the thickness of the composite [9, 13, 14]. For Camanho et al. [10], the first and most important damage is delamination between the composite plies but other authors consider that kinking is the critical damage that initiates the rest of the failure [15-18]. Another important parameter to be taken into account when dealing with a woven composite is the fiber waviness. The greater the undulations in the fibers, the greater the material's tendency for delamination [19, 11].

A preliminary experimental test campaign performed on the material showed that the damage leading to bearing failure in oxide/oxide CMC was similar to that in organic matrix composite [20, 21]. However, it was difficult to clearly determine the order of appearance of the damage. Therefore, a new test method was designed in order to monitor the damage development in the bearing plane and to obtain a damage chronology for the bearing behavior. Two different stacking sequences were studied and the influence of the fiber waviness was investigated.

Material and experimental protocol

Material

The material studied was a woven composite laminate with an 8 harness satin wave ply, produced by Safran Ceramics. It is composed of alumina fibers (Nextel™ 610) and an alumina matrix. No fiber interface coating was applied. The manufacturing process of the composite began with the infiltration of alumina plies with a slurry containing ceramic particles. Then the fabric was dried at low pressure, and partial sintering was performed in order to obtain a material with 25-30% microporosity. Such processing can induce defects in the composite before the tests, such as matrix micro-cracks and macropores [5]. Eight specimens were tested, with two different stacking sequences: [0]₁₀ and [0/45/0/45/0]_s. Every specimen was examined with an SEM and with C-scans before the tests in order to spot potential defects.

Figure 1: Modified bearing sample based on ASTM D5961 [22]

Sample design

In the preliminary test campaign on standard bearing specimens to characterize the damage development in oxide/oxide CMC [20, 21], the tests were stopped at different bearing phases in order to obtain a damage chronology. It was shown that some damage appeared on the load drop, as V shaped damage on the bearing plane [20, 21]. These observations provided first indications but were not sufficient and it was quite difficult to stop the tests at different points of the load drop stage. Moreover, to observe the damage on the bearing zone with an SEM, it was necessary to cut the specimen. This operation could potentially introduce additional defects, and it was therefore complex to discriminate the source of the observed damage.

Consequently, a new experimental procedure needed to be designed to allow direct observation of the bearing plane during the tests (Figure 1). Schilling et al. [23] performed tests on a full bearing specimen with in situ tomography but this solution was expensive and required a complex test setup. Aldebert et al. [24] and Catché et al. [25] studied the damage chronology on the slice of a rectangular composite plate, with an adjusted axis producing a compressive load on the slice. While this setup allowed for the monitoring of the bearing zone, it did not consider the drilling effects (surface roughness, local damage) or the stress intensity factor due to the hole, and the contact area between the axis and the plies was not representative of a bolted joint.

In this paper, the geometry was therefore adapted so as to obtain a contact zone that was more representative of a bearing test (Figure 2). The setup was designed with two drillings in order to be symmetric. This improved the stability of the specimen, prevented sliding during the test and ensured a quasi-simultaneous failure of the two partial holes. Even when simultaneity was not achieved, the setup still had the interest of allowing access to a history of the bearing damage. This symmetric behavior was monitored thanks to digital image correlation monitoring, by checking that the vertical displacement of the specimen was equivalent on both sides. Moreover, the geometry of the specimen, particularly its free length, ensured that the failure would be a bearing one.

Figure 2: Sample geometry

Tests conditions and instrumentation

The sample was held at its top by an adjustment system that allowed it to be rebalanced at the beginning of the tests. The bearing contact was achieved with two axes made of steel, to which a compression load was applied (Figure 3.a). Monotonic tests were performed on an Instron 100 kN with controlled displacement. The specimens were loaded at a rate of 0.1 mm/min, at room temperature. The damage development on both slices was monitored in real time with two high speed cameras (Photron FASTCAM SA5 and MINI AX200) taking 100 000 frames per second. This rate of acquisition was chosen before the tests to be sure to record enough data during the load drop phase (about 5 ms). An analysis of the results showed that it could be lowered to 20 000 frames per second without loss of information. The two high speed cameras were synchronized, and the load was recorded in order to be correlated with the pictures taken by the devices. In addition, a digital image

correlation setup (VIC 3D) was used to measure displacement and strain on the front face of the specimen. The test configuration is presented in Figure 3.b.

Figure 3: Experimental design (a) test setup and (b) instrumentation

After the tests, an SEM was used to obtain a final cartography of bearing damage inside the holes (area A) and on the slices (area B). Figure 4 is a schematic representation of the areas observed with the high speed cameras and studied with the SEM.

Figure 4: Areas observed with the experimental instrumentation of the BQH test

Experimental results

1) Global mechanical behavior

The experimental load versus displacement curves are presented in Figure 5. Four tests were performed for each lay-up. Figure 5.a corresponds to the $[0]_{10}$ stacking sequence (BQH₁₁, BQH₁₂, BQH₁₃ and BQH₁₄) and Figure 5.b to the $[0/45/0/45/0]_s$ one (BQH₂₁, BQH₂₂, BQH₃₂ and BQH₃₃). The mean maximum load was similar for both stacking sequences but the dispersion of the results was greater for the $[0/45/0/45/0]_s$ specimens. The curves can be decomposed into several stages, presented on one typical curve in Figure 6.

1. Adjustment of the specimen in the test setup (due to clearances)
2. Elastic linear behavior
3. Nonlinear behavior
4. First bearing peak and load drop
5. Load recovery
6. Second bearing peak and load drop
7. Residual load

Figure 5: Experimental curves for the BQH tests: (a) stacking sequence $[0]_{10}$ and (b) stacking sequence $[0/45/0/45/0]_s$

Figure 6: Phases of the BQH experimental behavior (BQH22)

These stages are quite similar to the ones occurring in a bearing test [20, 21], with a linear behavior stage, the appearance of non linearities due to the first damage, a brutal load drop after the peaks, and a residual load. The main difference is that there are two peaks, corresponding to the bearing failure of each partial hole. Even though the setup was designed to be as symmetrical as possible, the holes did not fail at the same time during the tests, although their failures were quite close. This can also be

explained by the fact that the microstructure of the material (the fiber waviness or the distribution of the macro-porosities) is likely to have been different on each side of the composite.

2) Damage chronology

The main damage observed was comparable to that existing in a classical bearing test [10, 20, 21]: fiber micro-buckling and kink bands, matrix cracking and delamination between adjacent plies (Figure 7).

Figure 7: SEM images (area B) of damage in the oxide/oxide CMC ($[0]_{10}$ specimen): (a) kink bands due to fiber buckling, (b) matrix cracks and (c) delamination between plies

Fiber pull-outs were noticeable, proving the efficiency of the weak matrix concept (Figure 8). Some fibers were also extracted from the slice (Figure 9). Unlike a standard specimen, the BQH did not have a closed bearing plane (free edge configuration), so there was no material to retain the fibers in the composite. This fiber extraction constituted additional damage that was not representative of the bearing chronology, and it will not be included in the damage chronology.

Figure 8: SEM image (area A) of fiber pull-out in a $[0/45/0/45/0]_s$ specimen

Figure 9: SEM image (area B) of fiber extraction from the slice of a $[0/45/0/45/0]_s$ specimen

The damage evolution on the slice of the specimens is presented in Figure 10 and Figure 11. Each image, taken with either the high speed camera or the SEM, shows the damage cartography at a bearing stage. It can be noted that the damage is localized on the external plies of the structure, regardless of the stacking sequence. This can be explained by the fact that the internal plies are contained by the external ones, so the damage evolution is restrained inside the composite.

Figure 10: Damage chronology for the $[0]_{10}$ specimens: (a) before testing (SEM image), (b) first matrix cracks (phase 3, high speed camera image), (c) propagation of matrix cracks and delamination through the thickness (phase 4, high speed camera image), and (d) specimen after the bearing failure (phase 7, SEM image)

Figure 11: Damage chronology for the $[0/45/0/45/0]_s$ specimens: (a) before testing (SEM image), (b) first matrix cracks (phase 3, high speed camera image), (c) propagation of matrix cracks and delamination at the $0^\circ/45^\circ$ interfaces (phase 4, high speed camera image) and (d) specimen after the bearing failure (phase 7, SEM image)

The damage chronology is quite similar for both stacking sequences. During phase 1 and phase 2, no damage is observed. The first degradation is seen in phase 3, which is consistent with the loss of linearity in the load-displacement curve. The first damage is fiber buckling in the 0° plies (Figures

10.b and 11.b). It can appear on either the internal or external plies, but always close to the contact area between the specimen and the steel axis. This damage is not easily detectable because of the camera resolution, but it seems to exist in several specimens.

At the end of phase 3, matrix cracks appear on the slice of the composite, along the longitudinal tows. These cracks do not always emerge at the same location, and sometimes develop millimeters away from the contact zone.

The load drop (phase 4) corresponds to the swelling of the structure induced by the development of new matrix cracks and the propagation of the former one. The damage during this phase is described more precisely in the next section. The weakening of the structure then leads to the appearance of ply buckling, delamination and kink bands, causing the final failure. In several specimens, delaminations are not distributed throughout the thickness but appear first on the external plies of the composite. Then they propagate through the thickness towards the internal plies by following the shape of the fiber tows (Figure 11.c). On the SEM image taken after the tests, it can be seen that the extent of the delamination is greater in the external plies than in the internal ones, and that the final degradation is V shaped (Figure 11.d).

3) **Damage kinematics during the load drop phase**

The damage development during stage 4 of the BQH test was precisely studied with the images taken by the high speed cameras. The load displacement curves of two $[0/45/0/45/0]_s$ specimens can be seen on Figures 12 and 13. Figure 14 and Figure 15 show the mechanical behavior of two specimens exhibiting different degradation patterns.

Figure 12: Load displacement curve of BQH₂₂ during phase 4

Figure 13: Load displacement curve of BQH₃₃ during phase 4

On Figure 14, the two first images of the BQH₂₂ load drop phase show that some damage (matrix cracks and delamination of an external ply) existed before this stage. During the falling of the load, the delamination extends, new matrix cracks and delamination appear and the existing ones propagate along the composite (images 4.c to 4.f). It can also be observed that the swelling of the slice occurs during this phase (between images 4.e and 4.f). Finally, at the end of this sequence, the initial delamination leads to the buckling of the external ply of the specimen.

Figure 14: High speed camera images of damage kinematics (delamination propagation) during the load drop stage (BQH₂₂)

Images 4.a and 4.b of Figure 15 also prove that damage (matrix cracks) occurred before phase 4. Then, in images 4.c to 4.g, corresponding to the sudden load drop, they propagate and new, similar damage is created. This propagation tends to be greater on the external plies, and a global V-shaped

degradation is visible on image 4.i. Similarly to BQH₂₂, the swelling of the composite occurs at the beginning of the fall (between images 4.c and 4.d).

Figure 15: High speed camera images of damage kinematics (delamination propagation) during the load drop stage (BQH₃₃)

4) Comparison of two tests

The damage development can be linked with the macroscopic behavior. In this section, two specimens presenting the same stacking sequence ([0/45/0/45/0]_s) are studied. BQH₂₁ has a higher stiffness before breakage than BQH₃₃ but a lower bearing peak load (Figure 16).

Figure 16: Experimental curves for the BQH₂₁ and BQH₃₃

The pictures from the high speed cameras indicate that BQH₃₃ shows cracks almost at the beginning of phase 2, whereas BQH₂₁ exhibits its first damage later (Figure 17). The stiffness degradation being linked with the composite damage, the former specimen maintains its initial stiffness longer than BQH₃₃. The images at the bearing point also show differences between the two specimens (Figure 18). Both samples exhibit several delaminations but, on the BQH₂₁, their extent is greater. The damage must have propagated faster and more easily on this specimen, causing a premature failure.

Figure 17: High speed camera images of the specimens at the beginning of phase 2: (a) BQH₂₁ and (b) BQH₃₃

Figure 18: High speed camera images of the specimens at the first bearing peak (phase 4): (a) BQH₂₁ and (b) BQH₃₃

Discussion

1) Influence of the material microstructure

The behavior of the two stacking sequences exhibited several similarities for damage development. The same damage was noted at the same stages for both lay-ups. The dispersion of the results seems to be linked to the material microstructure rather than to the lay-up.

The presence of a privileged zone for damage appearance and propagation was found on some specimens. These zones corresponded to locations where the fiber waviness and therefore the matrix fraction were the most marked. On Figure 19, it is noticeable that the first matrix cracks occur at a place where the fiber waviness induces a surplus of matrix and, on Figure 20, the delamination of the composite propagates over a similar area.

Two phenomena can explain this observation. Firstly, the matrix is less resistant than the fibers in this material, so the matrix surplus in these areas weakens the structure locally and promotes the emergence of the first material degradations. Moreover, the fiber waviness induces a geometric perturbation. The fibers are pre-buckled, so a smaller stress is sufficient to lead to the buckling of the plies.

Figure 19: Damage appearance related to the microstructure: (a) before testing, location of the highest matrix fraction (SEM, area B) and (b) during the test, location of the first matrix crack (high speed camera)

Figure 20: Damage appearance related to the microstructure: (a) before testing, location of the highest matrix fraction (SEM, area B) and (b), during the test, propagation of a delamination (high speed camera)

2) Influence of the composite machining

The location of the bearing damage can also be influenced by the machining of a composite, which can cause defects such as fiber extraction or matrix breakage, and these can initiate the first damage when the specimen is subjected to a bearing load [26-28]. Figure 21 shows an example of such a phenomenon. The post mortem SEM picture shows that some 0° tows were broken on the bearing contact area. A comparison with the pre-test SEM image reveals that the location of such breakage corresponds to the place where the fibers were damaged by the drilling. On Figure 22, the first matrix crack seems to coincide with fiber degradation due to the cutting operation.

Figure 21: SEM images (area A) of BQH specimens, the machining defects induce tow breakage (a) image before testing and (b) image after the experiment

Figure 22: Images of BQH specimens; the machining defects induce cracks (a) Image before testing (SEM, area B) and (b) image during the experiment (high speed camera)

3) Comparison with a standard bearing test

The results obtained were compared to those of standard bearing tests in order to assess the relevance of our experimental design. The comparison was made for $[0/45/0/45/0]_s$ specimens, as the available bearing tests were performed with this stacking sequence. Figure 23 shows the bearing specimen geometry and loading conditions. The width of the BQH specimen is smaller than the standard one but both have bearing failure so the qualitative results can be compared.

Figure 23: Bearing specimen geometry and loading conditions (DIC image)

Load-displacement curves

The load-displacement curves of two representative specimens for standard bearing and BQH experiments are plotted in Figure 24. The maximum load is 25% higher on average for the standard test. This can be explained by the fact that the contact zone is smaller with the quarter hole device, the axis only pushing on a partial bearing zone. Moreover, the geometry of the specimens is not the same and this parameter can influence the ultimate load in a bolted joint [8, 29, 30]. Unlike the standard bearing one, the BQH specimen also presents a free edge; hence the damage is not confined and can develop more easily. For the standard test, the stress at peak can be deduced from the relation $\sigma = (F/dt)$, where F is the load, t the thickness of the composite plate, and d the hole diameter. However, due to the specimen geometry, this relation is no longer applicable for the BQH device, and the bearing stress cannot be obtained from this test.

Figure 24: Experimental load displacement curves for standard bearing and BQH tests

Digital image correlation

The digital image correlation data were also compared, and the longitudinal strain cartographies at the first bearing point are presented in Figure 25. It can be seen that the cartographies are qualitatively similar: the digital image correlation shows that there is a strain location from the start of the nonlinear phase. This higher strain certainly indicates the appearance of damage in the composite. It is located near the bearing contact zone, over a distance nearly corresponding to the drilling diameter.

Figure 25: Longitudinal strain cartography (%) at the first bearing point: (a) standard bearing test, (b) BQH test

Moreover, the value of the longitudinal strain can be compared for both experiments along a vertical line located on the bearing plane (Figure 26). For the standard test, the curve is the one obtained at the bearing peak. For the BQH test, the cartographies of both bearing peaks are presented. The line L0 corresponds to the first bearing peak (for the left hole) and the line L1 to the second one (right hole). For both configurations the vertical position $y=0$ is taken next to the hole.

At the bearing location ($y=0$), all configurations show the same behavior, with a negative strain due to the compressive damage. The value of the strain for the standard bearing is included between those for the BQH test. It can be observed that the strain variation is different for the two bearing peaks of the BQH, but this can be explained by the different behaviors of the two holes. For L0, the study of the out of plane displacement indicates that the specimen is subjected to a local buckling on the external ply at the first bearing point (Figure 27). This may explain the fact that the longitudinal strain oscillates along the bearing plane and that its value is higher for $y=2$ than for $y=4$. In contrast, on the bearing plane L1, there is no buckling but only a swelling of the material on the bearing zone (Figure 28). These observations are confirmed by the camera images, with buckling appearing on the side of the DIC for L0 but only on the opposite side for L1.

Figure 26: Longitudinal strain as a function of the vertical position

Figure 27 : Out of plane displacement at the first bearing peak (BQH₂₂, L0)

Figure 28 : Out of plane displacement at the second bearing peak (BQH₂₂, L1)

When observing DIC results, some distinctions can be noted, in particular between the two holes of a BQH specimen. The two sides can break differently as the applied load cannot be entirely symmetric in the setup, and the DIC device only allows observation of one side of the specimen.

However, the DIC analysis shows that the BQH specimens behave in a similar way to the standard ones: the strains are similarly distributed at the bearing peaks, with equivalent values of strain for both configurations.

Damage observations

For both configurations, bearing damage was studied. Post mortem observations were achieved using an SEM, with images taken inside the hole (Figure 29, area C) and on the bearing plane (after cutting the specimen for the standard bearing tests, Figure 30, area D).

Figure 29: First SEM observation area (inside the hole)

Figure 30: Second SEM observation area (on the bearing plane/bearing zone)

Moreover, some X-ray tomographies were performed for the standard experiments. Regarding the BQH experiment, damage was also monitored with high speed camera images on the bearing plane. Several resemblances were noticed:

- The location of the main damage: on both configurations, the external plies were more damaged than the internal ones (Figure 31). Moreover, on some specimens, the external plies (0° plies) were broken due to a compression failure (Figure 32).

Figure 31: SEM images of the specimen after the tests, showing the external plies more damaged than the internal ones: (a) on a standard bearing test (area C) and (b) on a BQH test (area A)

Figure 32: SEM images of the breakage of the external plies: (a) on a standard bearing test (area D) and (b) on a BQH test (area B)

- On the SEM images, it can be seen that the edges of some 0° rows are missing, due to the buckling of the plies near the bearing contact (Figure 33)

Figure 33: SEM images of tow breakage: (a) on a standard bearing test (area D) and (b) on a BQH test (area A)

- There are fiber kink bands near the contact zone, on the bearing plane of the composite (Figure 34).

Figure 34: SEM images of kinking due to the bearing failure: (a) on a standard bearing test (area D) and (b) on a BQH test (area B)

- The same V-shaped damage can be observed through the thickness of the composite, on the bearing plane (Figure 35).

Figure 35: Damage after failure on the slice of the specimen: (a) tomography of the bearing plane on a standard bearing test and (b) high speed camera image on a BQH test

Stress distribution in the contact zone

Finite element analyses were performed on Abaqus in order to compare the stress distribution on the contact zone for BQH and bearing specimens for $[0/45/0/45/0]_s$ lay-up. The computation uses the Full Newton Raphson solver (ABAQUS General Standard) with nonlinear geometric activation.

The CMC specimen was meshed at ply level, with twenty quadratic C3D8 elements (Abaqus reference) per ply (brick elements with eight Gauss point and three DoF per nodes) and represents the half of the test specimen (Figure 36). For this computation, the CMC behavior was considered to be linear elastic. The pin axes were modeled by rigid quadrangular shell elements R3D4 (Abaqus reference). The contact between the two parts was modelled with a normal component (“hard” contact) and a tangential one (penalty contact with a friction coefficient of 0.3). Pin axes are considered the master and sample the slave.

The boundary conditions are representative of the two configurations. For each sample, pin axis was clamped and an imposed displacement equal to -0.1 mm was applied to the opposite face (Figure 36). The same model was used for the bearing and BQH samples, only the symmetric conditions on the x direction change.

A convergence study was performed in order to validate the FE model. The mesh density according to the thickness direction varies between one and thirty two elements. The results show for BHQ sample model and for out of plane stresses distribution (Figure 37), that convergence is obtained for twenty elements in the ply thickness. We used the same mesh for bearing sample model.

Figure 36: Numerical model of the configurations

Figure 37: Mesh convergence study for BHQ FE model.

To compare the mechanical behavior of both configurations, a delamination criterion [31] was calculated along a path created on the z axis:

$$f = (\sigma_{zz}/\sigma_{zz}^R)^2 + (\sigma_{xz}/\sigma_{xz}^R)^2 + (\sigma_{yz}/\sigma_{yz}^R)^2$$

The material delaminates when f exceeds the value 1. The values of σ_{zz}^R , σ_{xz}^R and σ_{yz}^R were obtained through a previous experimental campaign aimed at obtaining the mechanical parameters of the oxide/oxide CMC by testing it with tension, compression, or shearing tests. The results of the delamination criterion for a displacement corresponding to the bearing displacement are presented in Figure 38.

Figure38: Delamination criterion of both configurations for [0/45/0/45/0]_s stacking sequence

The results are consistent with the experimental observations; in particular, delamination occurs at the same locations as predicted by the criterion. For both tests, the CMC tends to delaminate at the 0°/45° interfaces, and the delamination is greater on the external plies due to the free boundary conditions.

It can be noted that the BQH criterion is quantitatively higher than the standard bearing one. This confirms that the free edge in the BQH test could enhance delamination depending on the layup. In some other configurations to be determined, delamination could become preponderant and such a BQH test could not be compared to standard bearing test. In contrast, some layups could exhibit no difference in terms of delamination criterion, as can be seen in Figure 39 for the [0]₁₀ stacking sequence. For this layup, the BQH setup does not enhance delamination, it even tends to reduce it on the external plies. However, even if there is no delamination, some intra ply debonding can be seen in the composite. Performing finite element simulations gave an insight into the order of magnitude of delamination differences due to the BQH test configuration.

Figure39: Delamination criterion of both configurations for [0]₁₀ stacking sequence

Validity of the BQH test

These different comparisons tend to validate the interest of the BQH device when it comes to the study of damage developing in the bearing plane of a composite. The similarities regarding the macroscopic behavior, the strain and numerical stress distributions or the type of damage prove that the same mechanical behavior appears in both experimental configurations.

It is also necessary to be aware of the limits of such an experiment. In the BQH device, the contact zone is not exactly the same as the bearing one, leading to a difference in the maximum load. This difference is also induced by the free edge in the BQH device, which cannot contain the damage as a standard bearing specimen would. This leads to fiber extraction from the slice of the specimen, damage that must not be taken into account for the bearing chronology. Depending on the stacking sequence, the BQH setup can also enhance the delamination between the plies, especially if there are 0°/45° interfaces. Moreover, in comparison with a standard bearing test, an additional flexion around

the z axis is induced by the setup configuration. However, this flexion does not seem to induce any marked effect in the analysis of bearing damage.

Conclusion

The bearing failure mechanism of an oxide/oxide CMC was investigated through an experimental campaign. An original test set up was designed in order to obtain an accurate damage chronology of the material, with direct visual observation of the bearing plane. This new experimental design also brought additional information for modelling the bearing mechanical behavior by making the cracks easier to follow.

The bearing failure is due to an accumulation of multiple degradations including kink bands, matrix cracks and delamination. The first significant damage seems to be matrix cracking. The microstructure of the material plays an important role in the damage initiation as the cracks tend to appear on the zones with the highest matrix fraction, which are weaker than the rest of the structure.

The setup developed in this study relies on a new specimen geometry with a bearing load applied to two partial holes. The BQH test presents some differences with a conventional bearing test as the contact zone is not exactly the same and an additional flexion appears during the tests. Moreover, the edge effects induce supplementary damage: fiber extraction from the slice of the composite. However, these differences were taken into account in the analysis. It is also important to note that the information deduced from the BQH tests remains qualitative. This setup was designed to obtain a damage scenario but cannot be used to determine the bearing stress of a material.

Some improvements could be added to the instrumentation of the test in order to obtain more information. The acquisition rate of the high speed camera was chosen before the tests, but it could be lowered in order to obtain a better resolution for the pictures. This would allow the propagation of cracks to be followed more precisely. It would also be interesting to use some digital image correlation on the slices of the specimen (in addition to the one on the front) to map the strain in this area too.

It could be relevant to investigate the consequences of a misalignment of the specimens in the BQH device. To decrease the calculation time, the first finite element model that was proposed in this paper was purely symmetric but modelling the whole device could allow the misalignment phenomenon to be studied.

Acknowledgement

The authors would like to thank Safran Ceramics for its scientific contribution to the subject and for supplying the test material.

References

1. Keller KA, Jefferson G, Kerans RJ. Oxide-Oxide composites. Handbook of Ceramic Composite 2005. p.377-421
2. Koch D, Tushtev K, Grathwohl G. Ceramic fiber composites: Experimental analysis and modeling of mechanical properties. Composite Science and Technology 2008; 68: 1165-1172
3. Zok FW, Levi CG. Mechanical properties of porous-matrix ceramic composites. Advanced Engineering Materials 2001; 3:15-23
4. Mattoni MA, Yang JY, Levi CG, Zok FW. Effects of matrix porosity on the mechanical properties of a porous-matrix, all-oxide ceramic composite. Journal of the American Ceramic Society 2001; 84 (11): 2594-2602

5. Ben Ramdane C. Etude et modélisation du comportement mécanique de CMC oxyde/oxyde . PhD thesis, Université de Bordeaux 2014
6. Simon RA. Progress in processing and performance of porous-matrix oxide/oxide composites. *International Journal of Applied Ceramic Society* 2005; 2(2): 141-149
7. Heimbs S, Schmeer S, Blaurock J, Steeger S. Static and dynamic failure behavior of bolted joints in carbon fibre composites. *Composites: Part A* 2013; 47: 91-101
8. Collings TA. The strength of bolted joints in multi-directional CFRP laminates. *Composites* 1977; 8(1): 43-55
9. Kelly G, Hallstrom S. Bearing strength of carbon fibre/epoxy laminates: effects of bolt-hole clearance. *Composites: Part B* 2004; 35: 331-343
10. Camanho PP, Lambert M. A design methodology for mechanically fastened joints in laminated composite materials. *Composites Science and Technology* 2006; 66: 3004-3020
11. Ben Ramdane C, Julian-Jankowiak A, Valle R, Renollet Y, Martin E, Diss P. Microstructure and mechanical behaviour of a NextelTM610/alumina weak matrix composite subjected to tensile and compressive loadings. *Journal of the European Ceramic Society* 2017; 37(8): 2919-2932
12. Jackson PR, Ruggles-Wrenn MB, Baek SS, Keller KA. Compressive creep behavior of an oxide-oxide ceramic composite with monazite fiber coating at elevated temperature. *Material Science and Engineering A* 2007; 454-455: 590-601
13. Wu PS, Sun CT. Modeling bearing failure initiation in pin-contact of composite laminates. *Mechanics of Materials* 1998; 29: 325-335
14. Wang HS, Hung CL, Chang FK. Bearing failure of bolted composite joints. Part I: experimental characterization. *Journal of Composite Materials* 1996; 30(12): 1284-1313.
15. Sola C, Castanie B, Michel L, Lachaud F, Delabie A, Mermoz E. On the role of kinking in the bearing failure of composite laminates. *Composite Structures* 2016; 141: 184-193
16. Seike S, Takao Y, Wang WX, Matsubara T. Bearing damage evolution of a pinned joint in CFRP laminates under repeated tensile loading. *International Journal of Fatigue* 2010; 32: 72-81
17. Xiao W, Ishikawa T. Bearing strength and failure behavior of bolted composite joints (Part I: experimental investigation). *Composites Science and Technology* 2005; 65: 1022-1031
18. Hirano N, Takao Y, Wang WX. Effects of temperature on the bearing strength of CF/epoxy pinned joints. *Composites Science and Technology* 2007 ; 41(3) : 335-351
19. Lachaud F, Piquet R, Aldebert G, Huet J, Michel L. Analyse du comportement mécanique des assemblages boulonnés composites à renforts tissés. *Revue des Composites et des Matériaux Avancés* 2014 ; 24(4) : 449-464
20. Broutelle M, Lachaud F, Dupleix-Couderc C, Daidie A. Comportement en matage de composites à matrice céramique oxyde/oxyde. JNC20, Champs-sur-Marnes, 18-30 June 2017.
21. Broutelle M, Lachaud F, Daidie A, Barriere L, Dupleix-Couderc C, Bouillon F. Mechanical behavior of oxide/oxide ceramic matrix composite bolted joints. ECCM 2018, Athens, 25-28 June 2018.
22. ASTM, «Standard Test Method for Bearing Response of Polymer Matrix Composite Laminates», 2010.
23. Schilling P, Karedla BR, Tatiparthi AK, Verges MA, Herrington. X-ray computed microtomography of internal damage in fiber reinforced matrix composites. *Composites Science and Technology* 2005 ; 65 : 2071-2078.
24. Aldebert G, Lachaud F, Huet J, Piquet R. Etude de la cinétique d'endommagement en matage des composites à renforts tissés. JNC17, Poitiers, 15-17 June 2011.
25. Catche S. Analyse des défauts de paroi de trou et de leur criticité sur la tenue mécanique des structures mécaniques percées. PhD thesis, Université de Toulouse 2013
26. Catche S, Piquet R, Lachaud F, Castanie B, Benaben A. Analysis of hole wall defects of drilled CFRP laminates. *Journal of Composite Materials* 2014; 49(10): 1223-1240
27. Persson E, Eriksson I, Zackrisson L. Effects of hole machining defects on strength and fatigue life of composite laminates. *Composites Part A* 1997; 28: 141-151.
28. Rahme P, Landon Y, Lachaud F, Piquet R, Lagarrigue. Delamination-free Drilling of Thick Composite Materials. *Composites Part A* 2015; 72, 148-159
29. Okutan B. The effects of geometric parameters on the failure strength for pin-loaded multi-directional fiber-glass reinforced epoxy laminate. *Composites Part B* 2002; 33: 567-578.

30. Caprino G, Squillace A, Giorleo G, Nele L, Rossi L. Pin and bolt bearing strength of fiberglass/aluminium laminates. *Composites Part A* 2005; 36: 1307-1315
31. Hashin Z. Failure criteria for unidirectional fiber composites. *Journal of Applied Mechanics* 1980; 47: 329-334.

Figure Captions

Figure 1: Modified bearing sample based on ASTM D5961 [22]

Figure 2: Sample geometry

Figure 3: Experimental design (a) test setup and (b) instrumentation

Figure 4: Areas observed with the experimental instrumentation of the BQH test

Figure 5: Experimental curves for the BQH tests

Figure 6: Phases of the BQH experimental behavior (BQH₂₂)

Figure 7: SEM images (area B) of damage in the oxide/oxide CMC ([0]₁₀ specimen): (a) kink bands due to fiber buckling, (b) matrix cracks and (c) delamination between plies

Figure 8: SEM image (area A) of fiber pull-out in a [0/45/0/45/0]_s specimen

Figure 9: SEM image (area B) of fiber extraction from the slice of a [0/45/0/45/0]_s specimen

Figure 10: Damage chronology for the [0]₁₀ specimens: (a) before testing (SEM image), (b) first matrix cracks (phase 3, high speed camera image), (c) propagation of matrix cracks and delamination through the thickness (phase 4, high speed camera image), and (d) specimen after the bearing failure (phase 7, SEM image)

Figure 11: Damage chronology for the [0/45/0/45/0]_s specimens: (a) before testing (SEM image), (b) first matrix cracks (phase 3, high speed camera image), (c) propagation of matrix cracks and delamination at the 0°/45° interfaces (phase 4, high speed camera image) and (d) specimen after the bearing failure (phase 7, SEM image)

Figure 12: Load displacement curve of BQH₂₂ during phase 4

Figure 13: Load displacement curve of BQH₃₃ during phase 4

Figure 14: High speed camera images of damage kinematics (delamination propagation) during the load drop stage (BQH₂₂)

Figure 15: High speed camera images of damage kinematics (delamination propagation) during the load drop stage (BQH₃₃)

Figure 16: Experimental curves for the BQH₂₁ and BQH₃₃

Figure 17: High speed camera images of the specimens at the beginning of phase 2: (a) BQH₂₁ and (b) BQH₃₃

Figure 18: High speed camera images of the specimens at the first bearing peak (phase 4): (a) BQH₂₁ and (b) BQH₃₃

Figure 19: Damage appearance related to the microstructure: (a) before testing, location of the highest matrix fraction (SEM, area B) and (b) during the test, location of the first matrix crack (high speed camera)

Figure 20: Damage appearance related to the microstructure: (a) before testing, location of the highest matrix fraction (SEM, area B) and (b), during the test, propagation of a delamination (high speed camera)

Figure 21: SEM images (area A) of BQH specimens, the machining defects induce tow breakage (a) image before testing and (b) image after the experiment

Figure 22: Images of BQH specimens; the machining defects induce cracks (a) Image before testing (SEM, area B) and (b) image during the experiment (high speed camera)

Figure 23: Bearing specimen geometry and loading conditions (DIC image)

Figure 24: Experimental load displacement curves for standard bearing and BQH tests

Figure 25: Longitudinal strain cartography (%) at the first bearing point: (a) standard bearing test, (b) BQH test

Figure 26: Longitudinal strain as a function of the vertical position

Figure 27 : Out of plane displacement at the first bearing peak (BQH₂₂, L0)

Figure 28 : Out of plane displacement at the second bearing peak (BQH₂₂, L1)

Figure 29: First SEM observation area (inside the hole)

Figure 30: Second SEM observation area (on the bearing plane/bearing zone)

Figure 31: SEM images of the specimen after the tests, showing the external plies more damaged than the internal ones: (a) on a standard bearing test (area C) and (b) on a BQH test (area A)

Figure 32: SEM images of the breakage of the external plies: (a) on a standard bearing test (area D) and (b) on a BQH test (area B)

Figure 33: SEM images of tow breakage: (a) on a standard bearing test (area D) and (b) on a BQH test (area A)

Figure 34: SEM images of kinking due to the bearing failure: (a) on a standard bearing test (area D) and (b) on a BQH test (area B)

Figure 35: Damage after failure on the slice of the specimen: (a) tomography of the bearing plane on a standard bearing test and (b) high speed camera image on a BQH test

Figure 36: Numerical model of the configurations

Figure 37: Mesh convergence study for BQH FE model.

Figure38: Delamination criterion of both configurations for [0/45/0/45/0]_s stacking sequence

Figure39: Delamination criterion of both configurations for [0]₁₀ stacking sequence

Figures

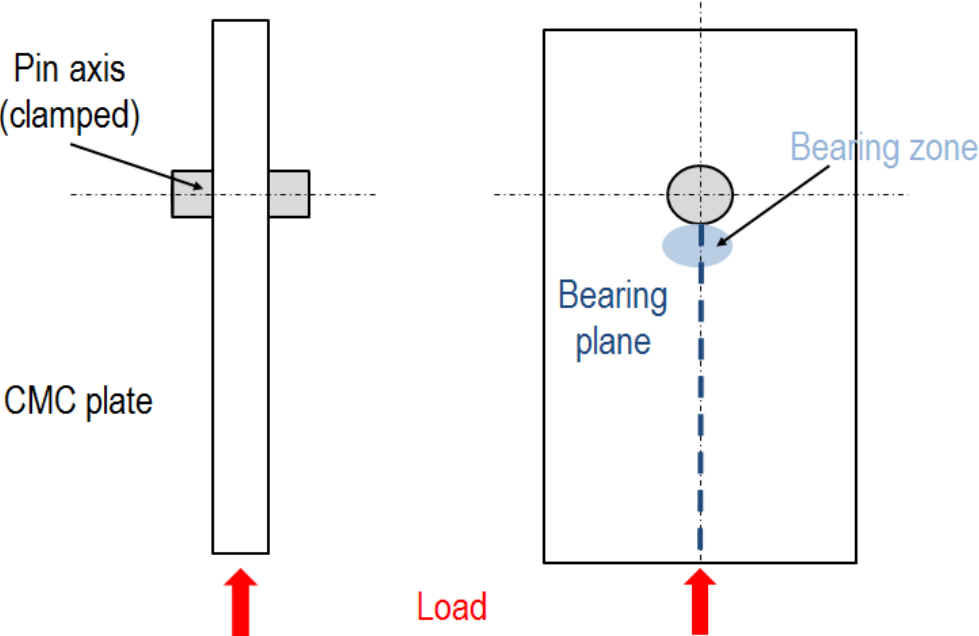


Figure 1: Modified bearing sample based on ASTM D5961 [22]

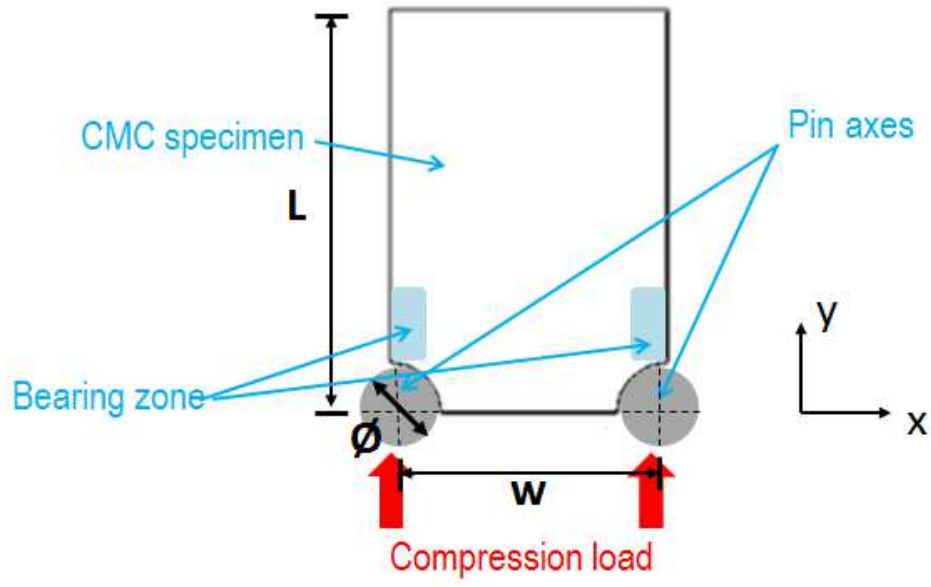


Figure 2: Sample geometry

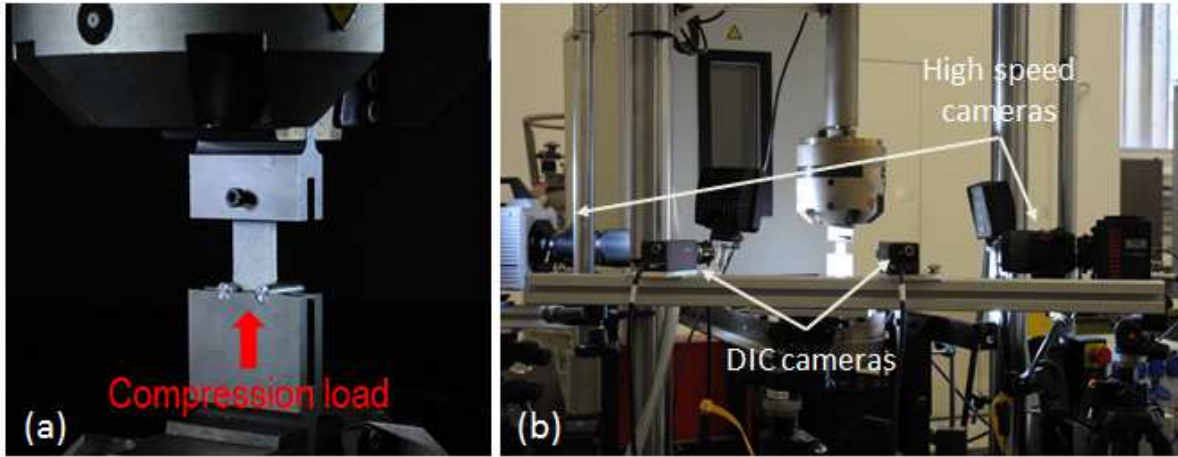


Figure 3: Experimental design (a) test setup and (b) instrumentation

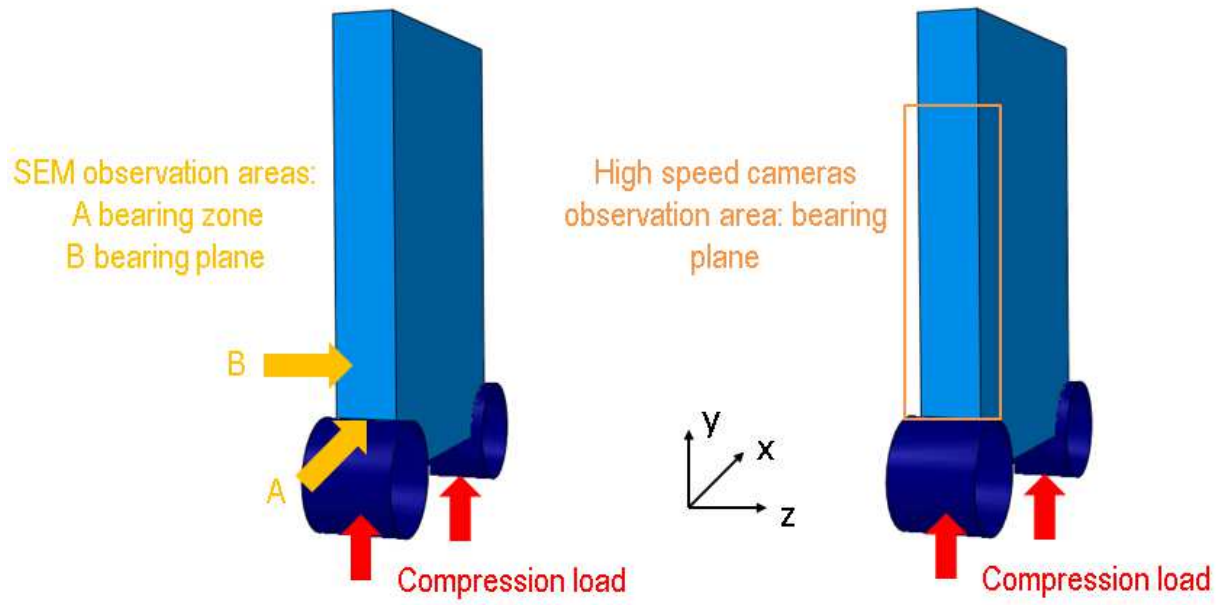


Figure 4: Areas observed with the experimental instrumentation of the BQH test

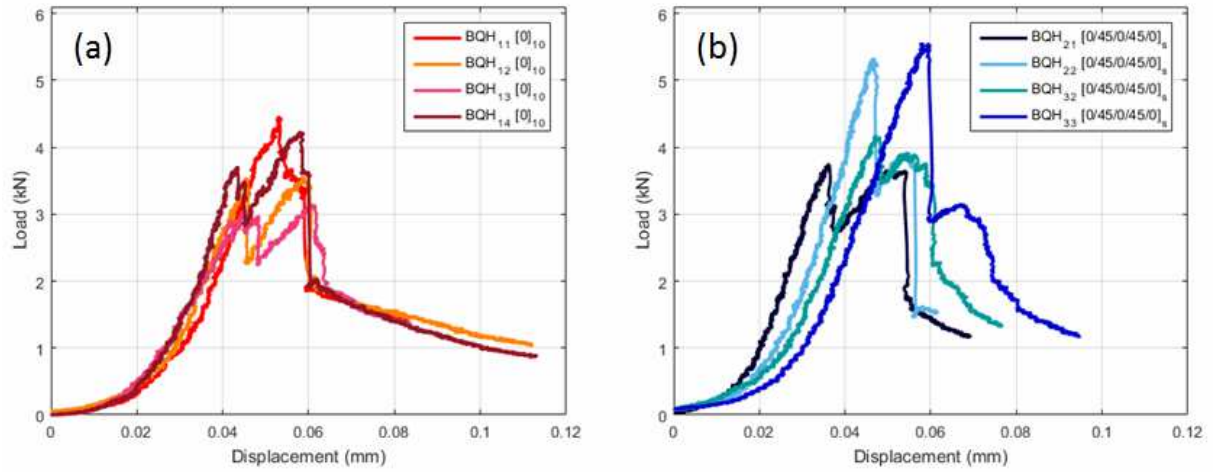


Figure 5: Experimental curves for the BQH tests: (a) stacking sequence $[0]_{10}$ and (b) stacking sequence $[0/45/0/45/0]_s$.

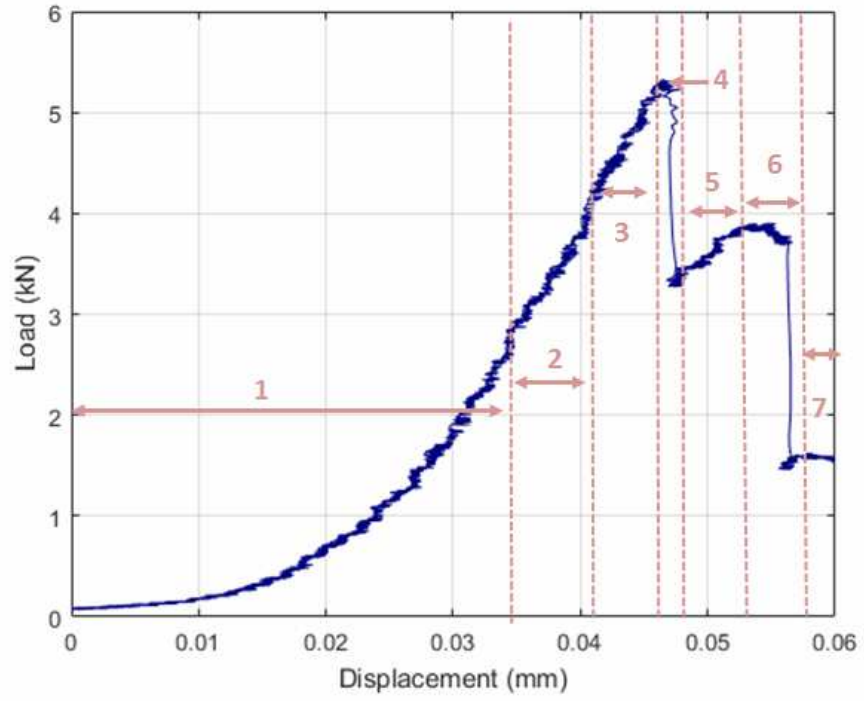


Figure 6: Phases of the BQH experimental behavior (BQH22)

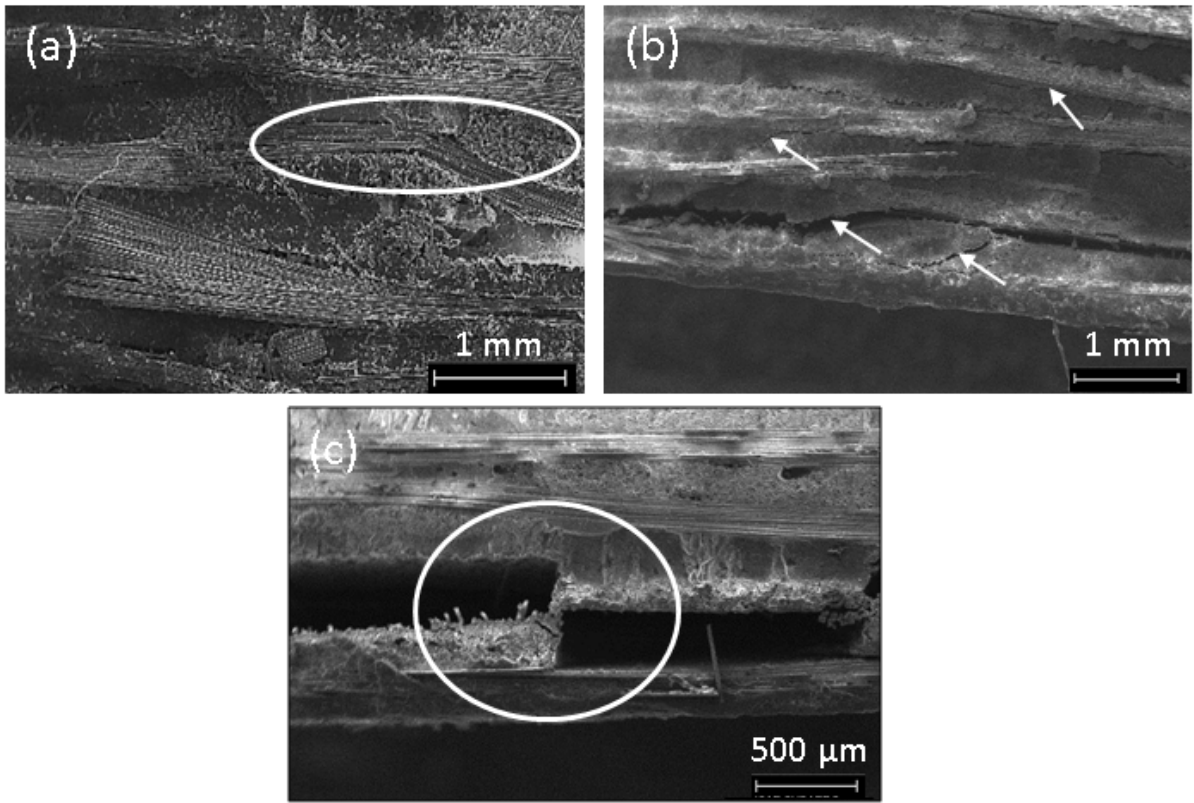


Figure 7: SEM images (area B) of damage in the oxide/oxide CMC ([0]₁₀ specimen): (a) kink bands due to fiber buckling, (b) matrix cracks and (c) delamination between plies

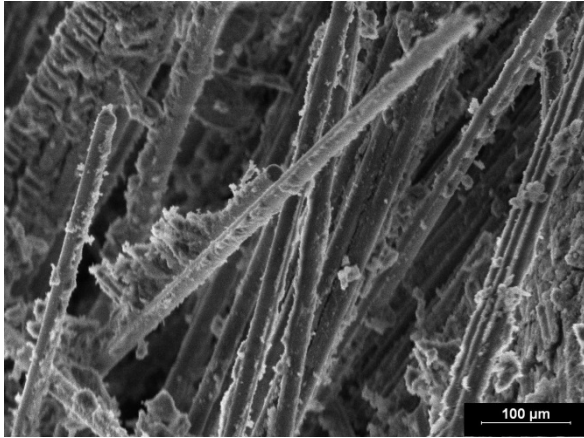


Figure 8: SEM image (area A) of fiber pull-out in a $[0/45/0/45/0]_s$ specimen

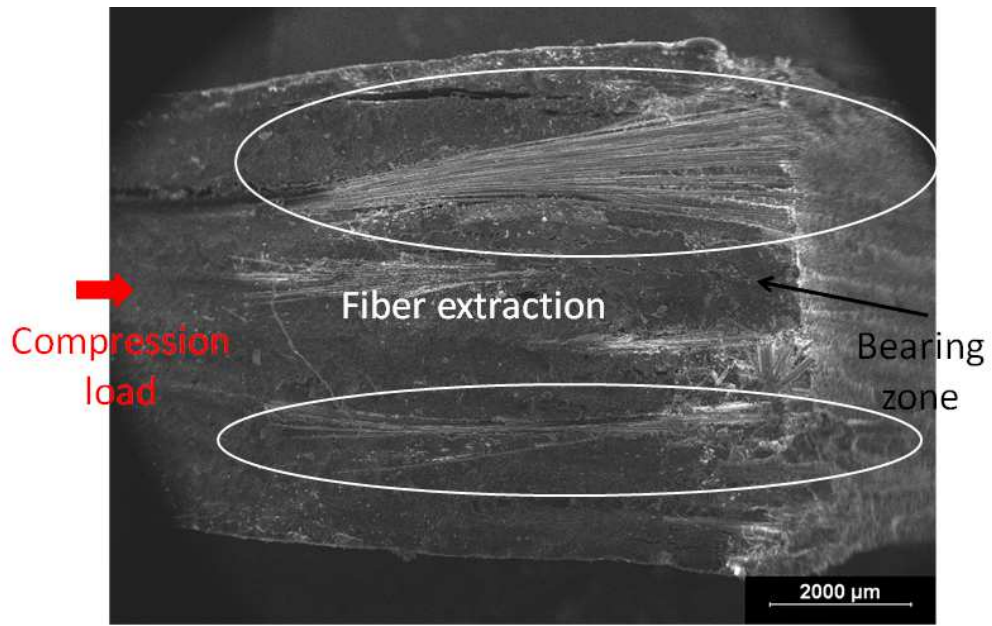


Figure 9: SEM image (area B) of fiber extraction from the slice of a $[0/45/0/45/0]_s$ specimen

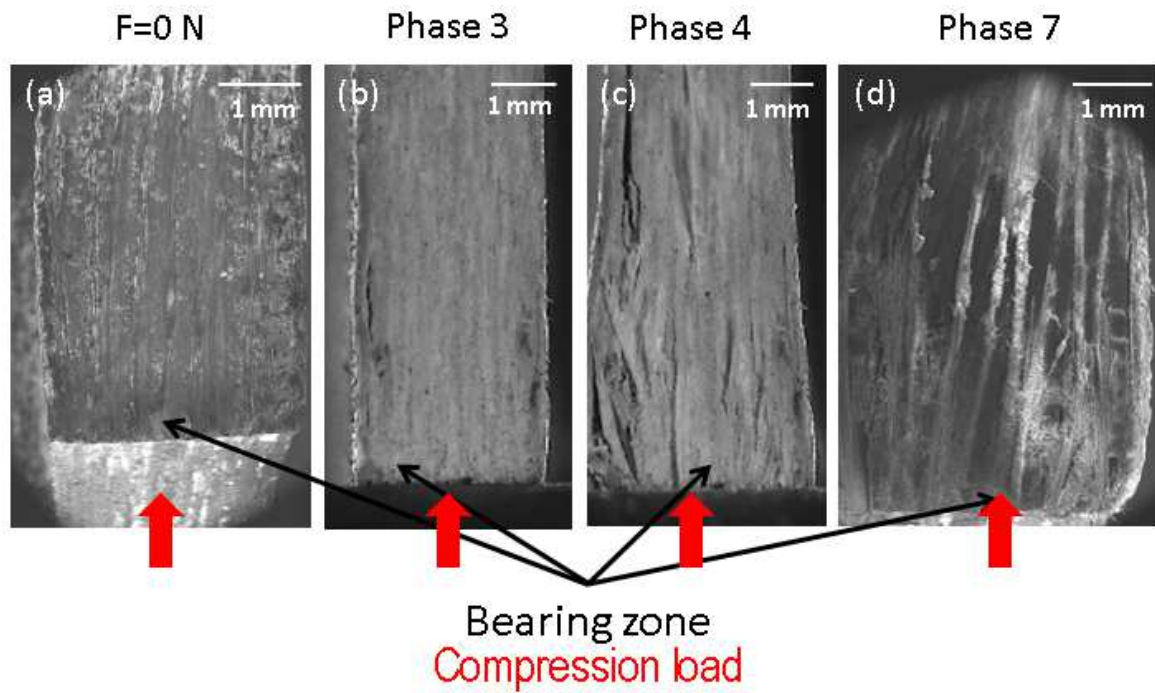


Figure 10: Damage chronology for the $[0]_{10}$ specimens: (a) before testing (SEM image), (b) first matrix cracks (phase 3, high speed camera image), (c) propagation of matrix cracks and delamination through the thickness (phase 4, high speed camera image,) and (d) specimen after the bearing failure (phase 7, SEM image)

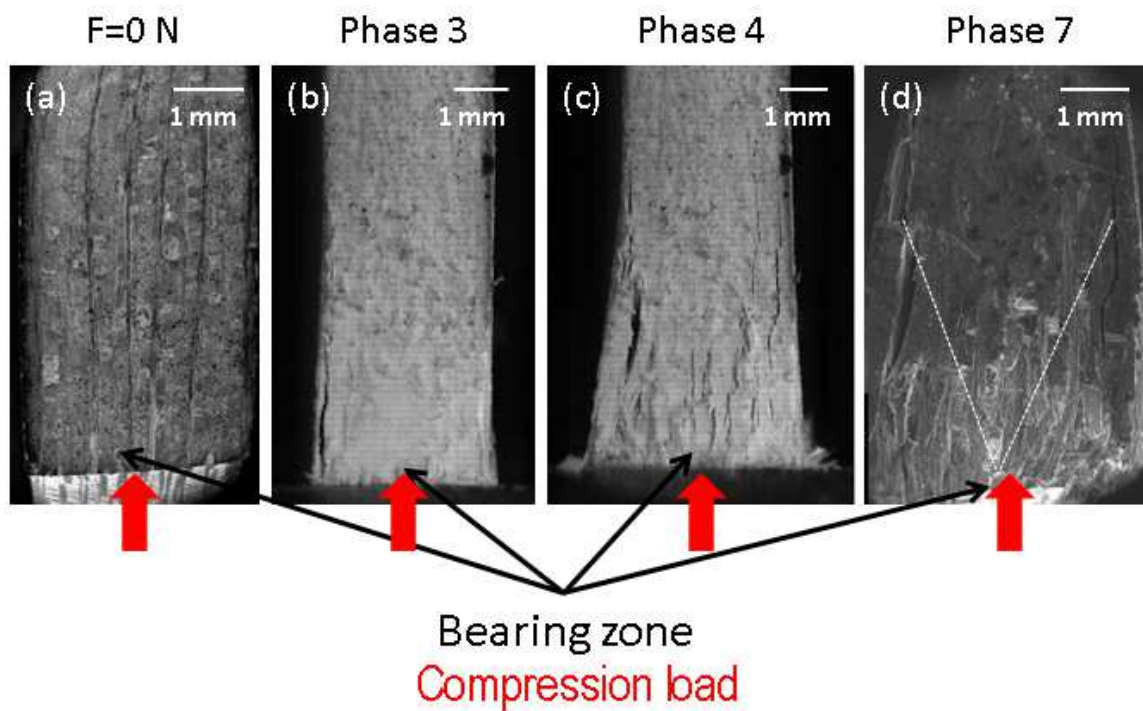


Figure 11: Damage chronology for the $[0/45/0/45/0]_s$ specimens: (a) before testing (SEM image), (b) first matrix cracks (phase 3, high speed camera image), (c) propagation of matrix cracks and delamination at the $0^\circ/45^\circ$ interfaces (phase 4, high speed camera image) and (d) specimen after the bearing failure (phase 7, SEM image)

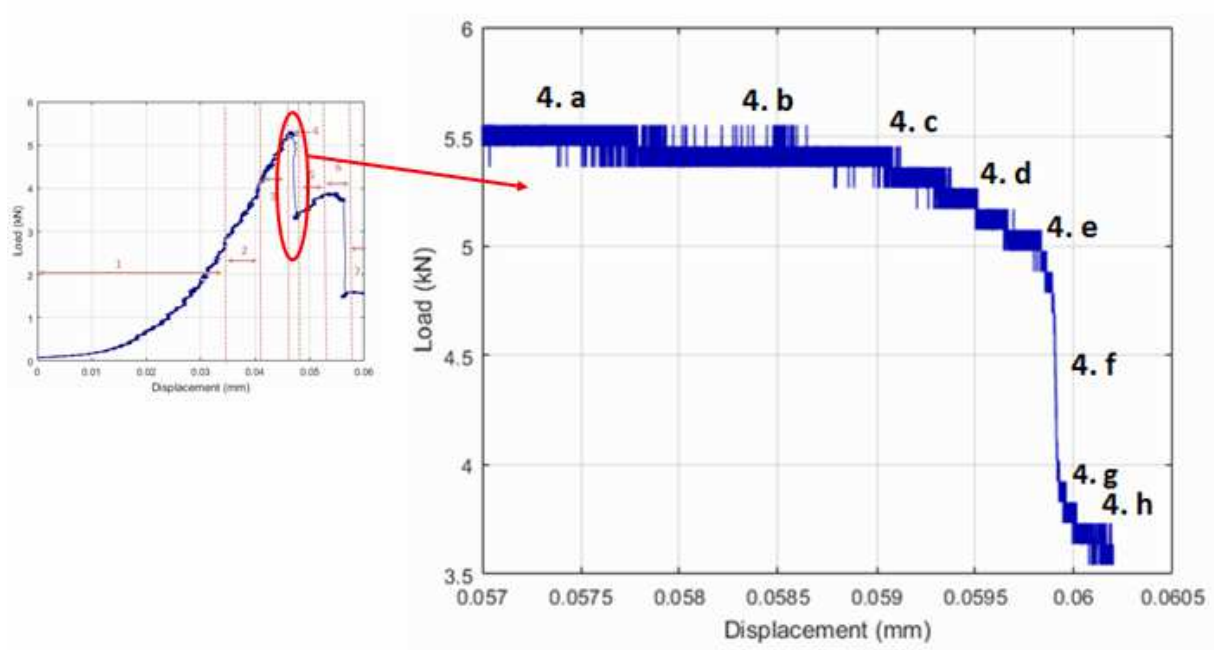


Figure 12: Load displacement curve of BQH₂₂ during phase 4

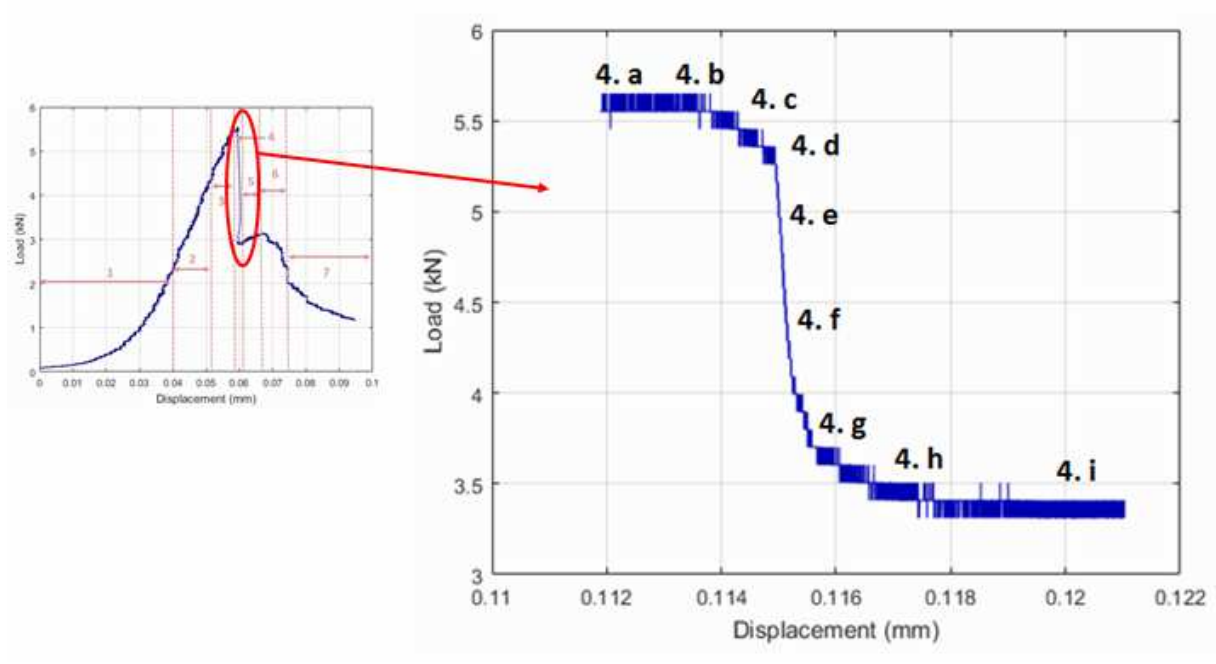


Figure 13: Load displacement curve of BQH₃₃ during phase 4

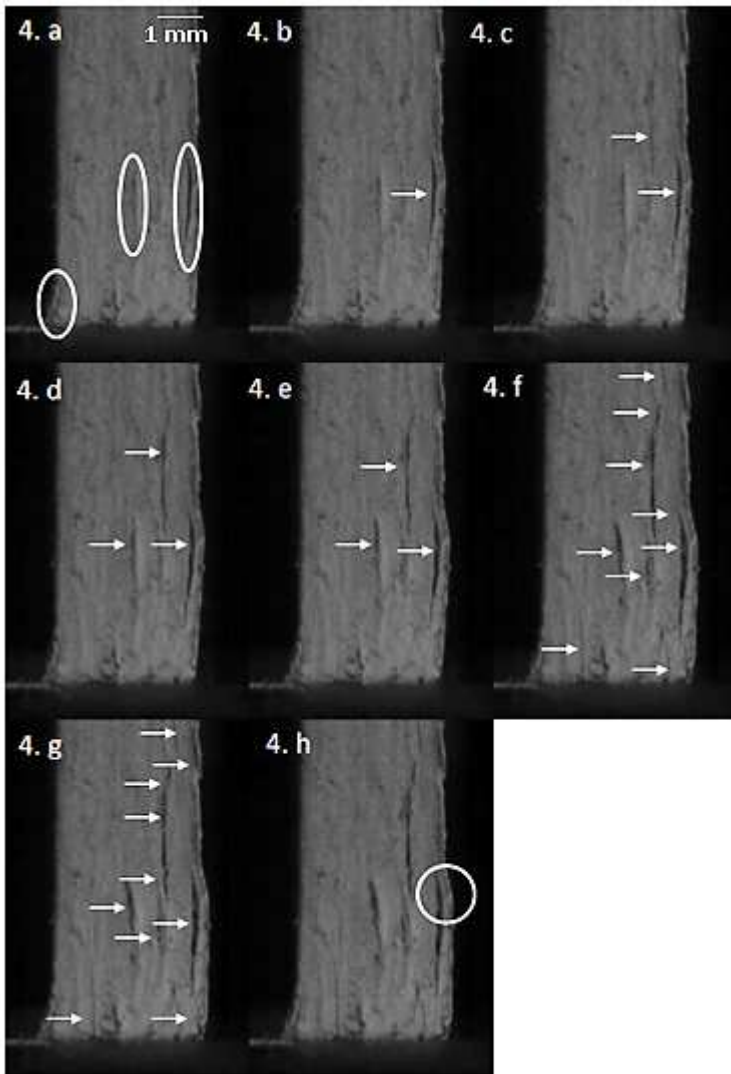


Figure 14: High speed camera images of damage kinematics (delamination propagation) during the load drop stage (BQH₂₂)

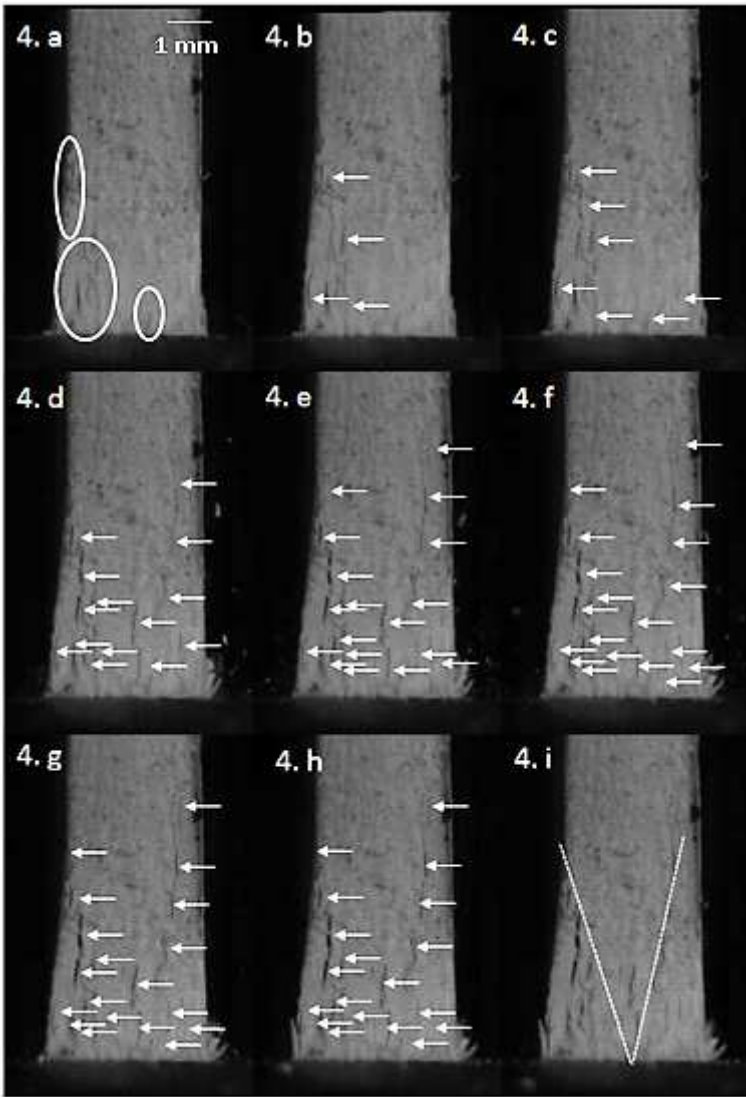


Figure 15: High speed camera images of damage kinematics (delamination propagation) during the load drop stage (BQH₃₃)

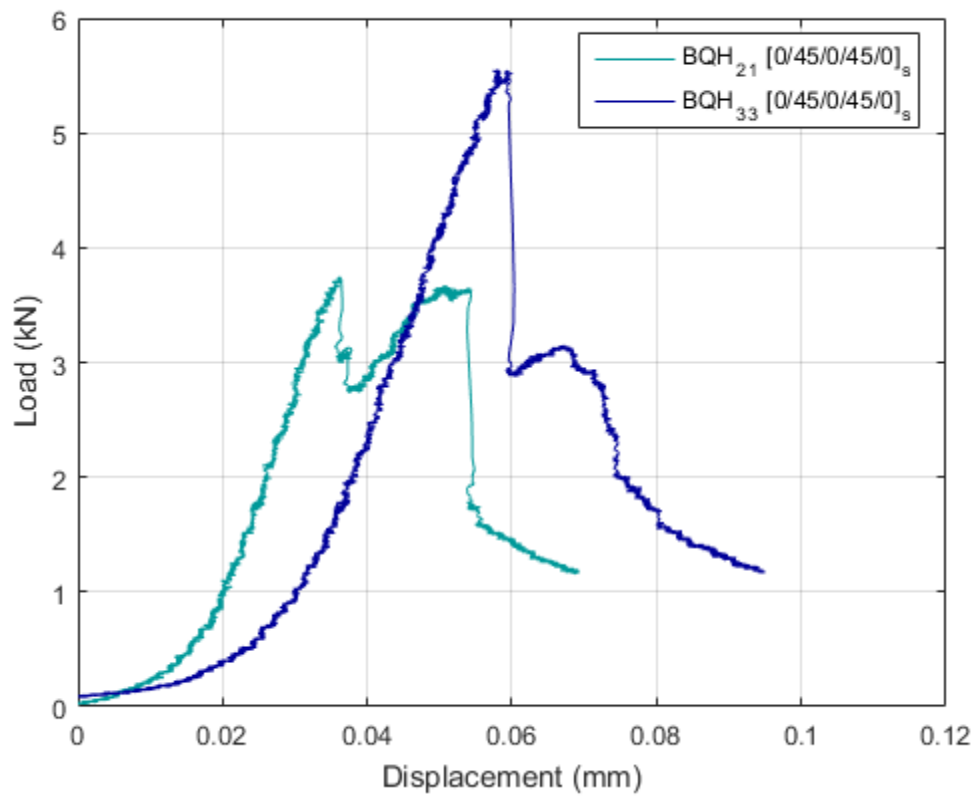


Figure 16: Experimental curves for the BQH₂₁ and BQH₃₃

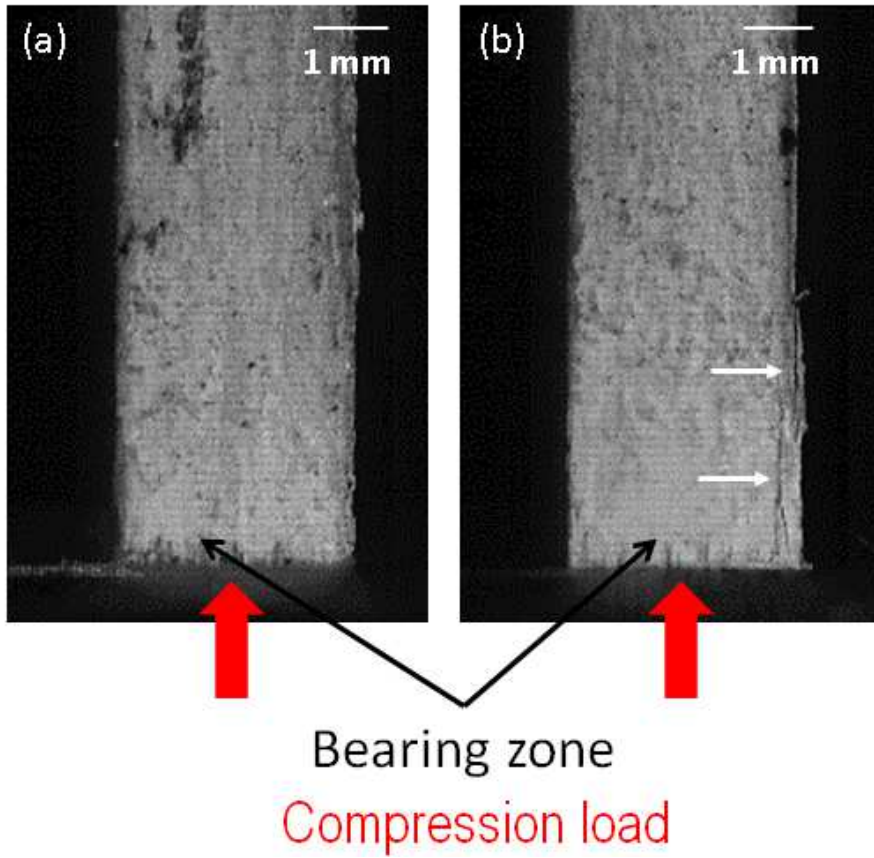


Figure 17: High speed camera images of the specimens at the beginning of phase 2: (a) BQH₂₁ and (b) BQH₃₃

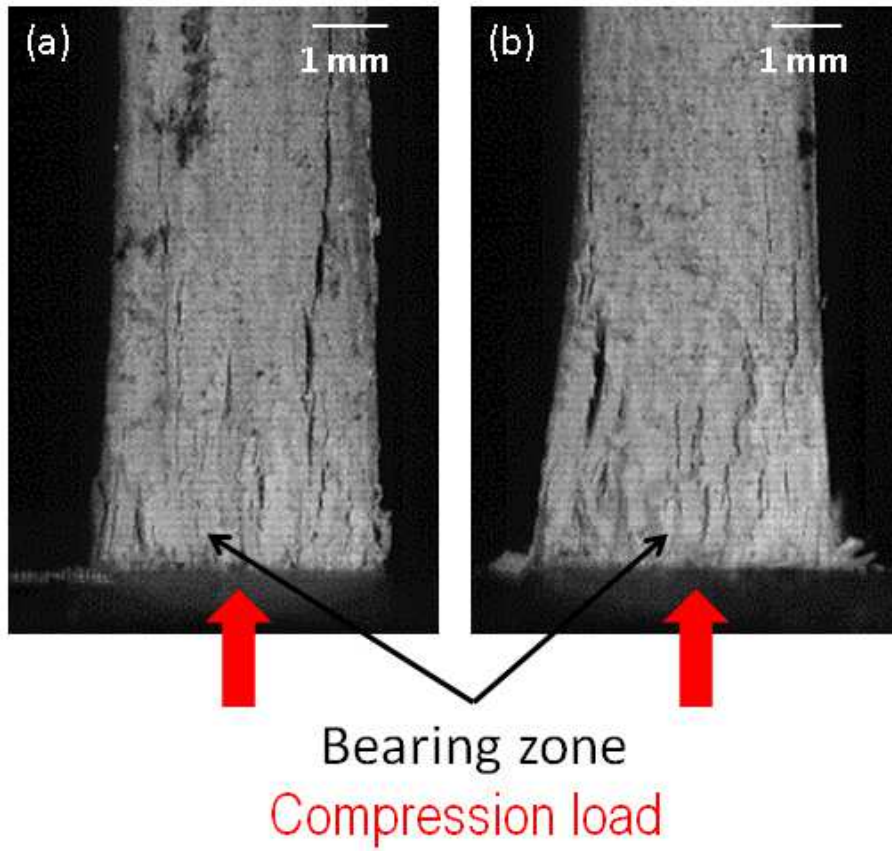


Figure 18: High speed camera images of the specimens at the first bearing peak (phase 4): (a) BQH₂₁ and (b) BQH₃₃

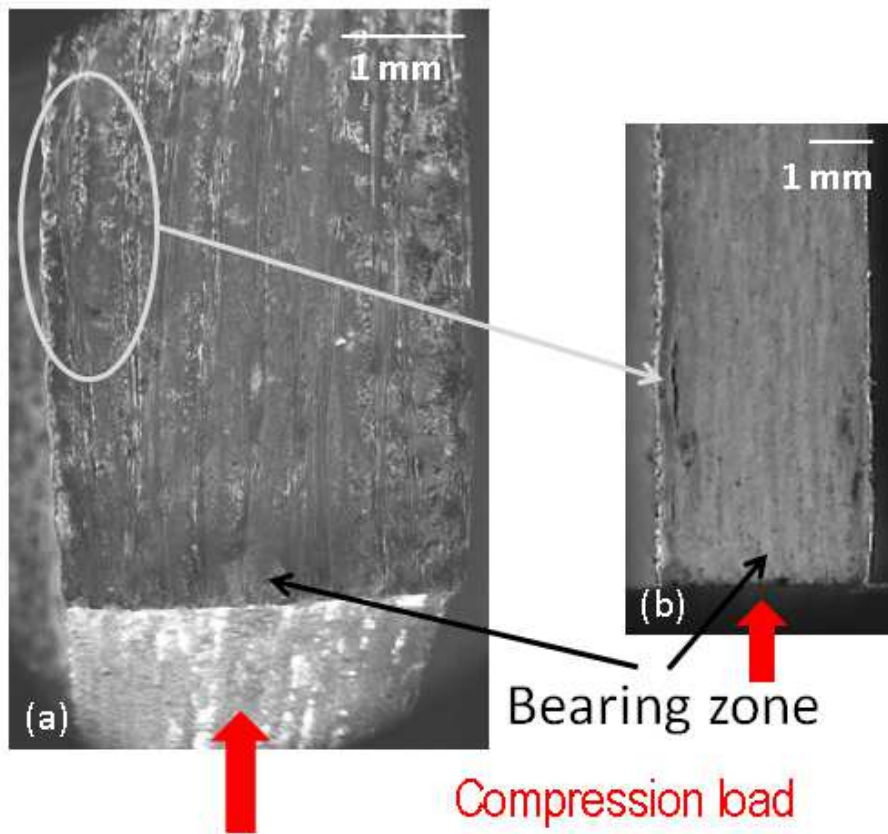


Figure 19: Damage appearance related to the microstructure: (a) before testing, location of the highest matrix fraction (SEM, area B) and (b) during the test, location of the first matrix crack (high speed camera)

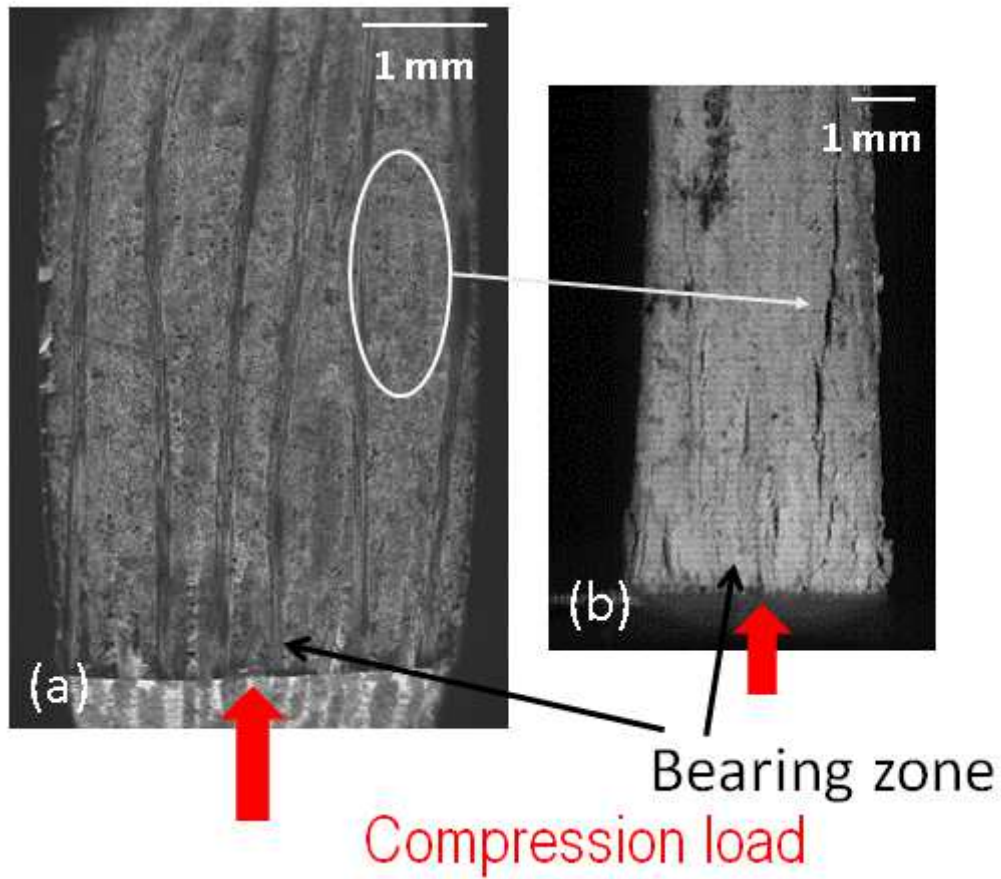


Figure 20: Damage appearance related to the microstructure: (a) before testing, location of the highest matrix fraction (SEM, area B) and (b), during the test, propagation of a delamination (high speed camera)

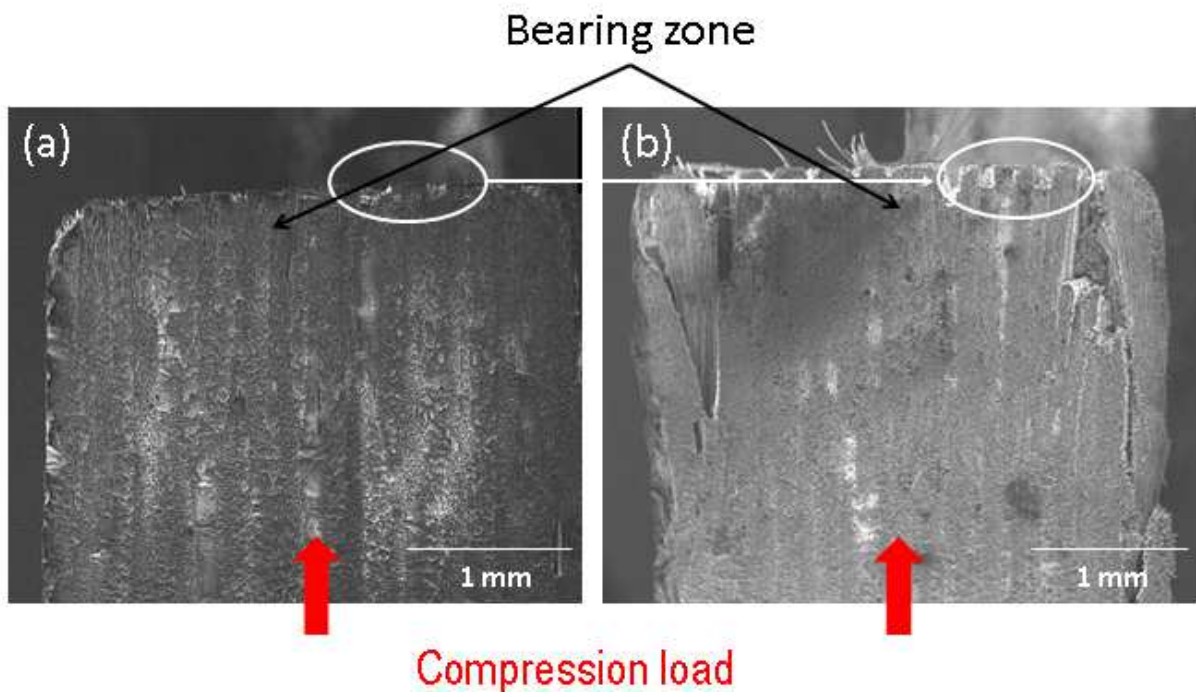


Figure 21: SEM images (area A) of BQH specimens, the machining defects induce tow breakage (a) image before testing and (b) image after the experiment

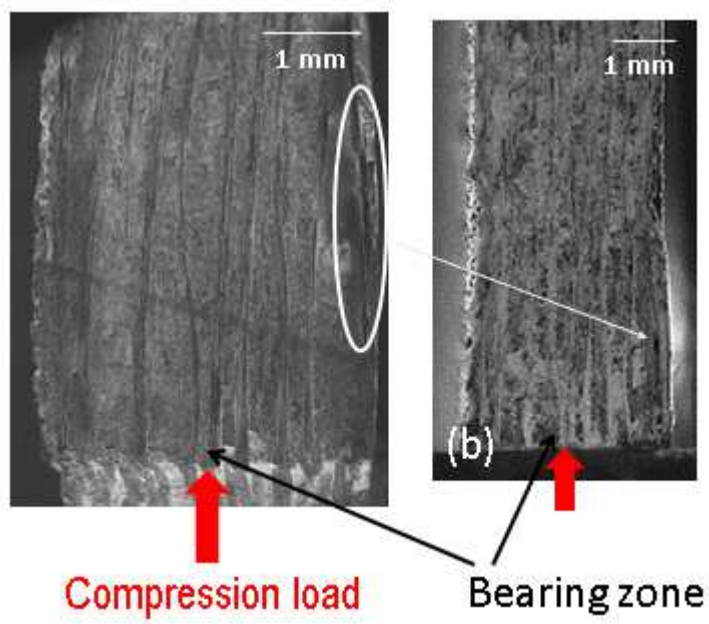


Figure 22: Images of BQH specimens; the machining defects induce cracks (a) Image before testing (SEM, area B) and (b) image during the experiment (high speed camera)

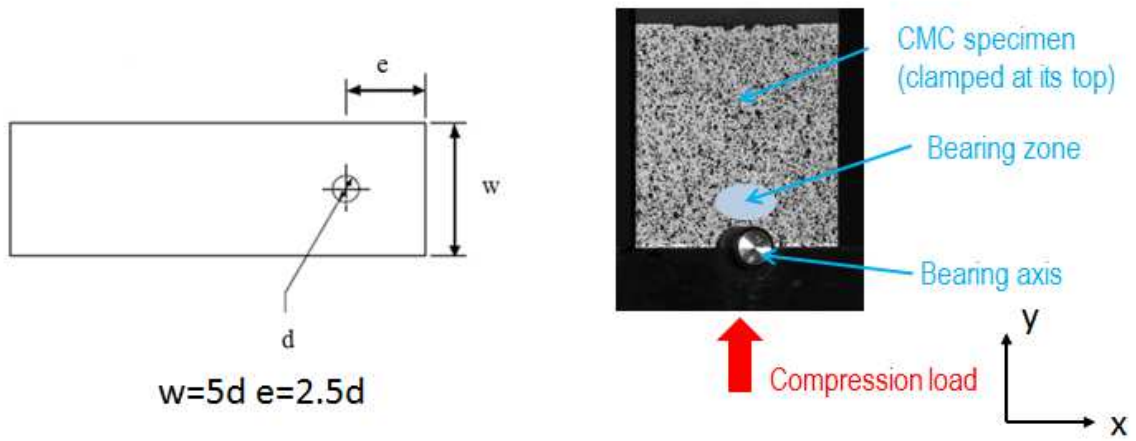


Figure 23: Bearing specimen geometry and loading conditions (DIC image)

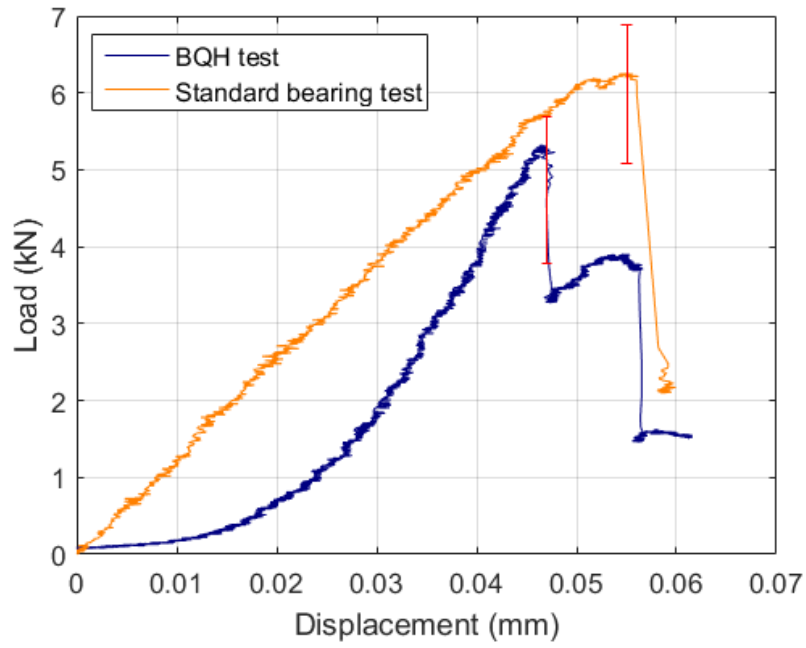


Figure 24: Experimental load displacement curves for standard bearing and BQH tests

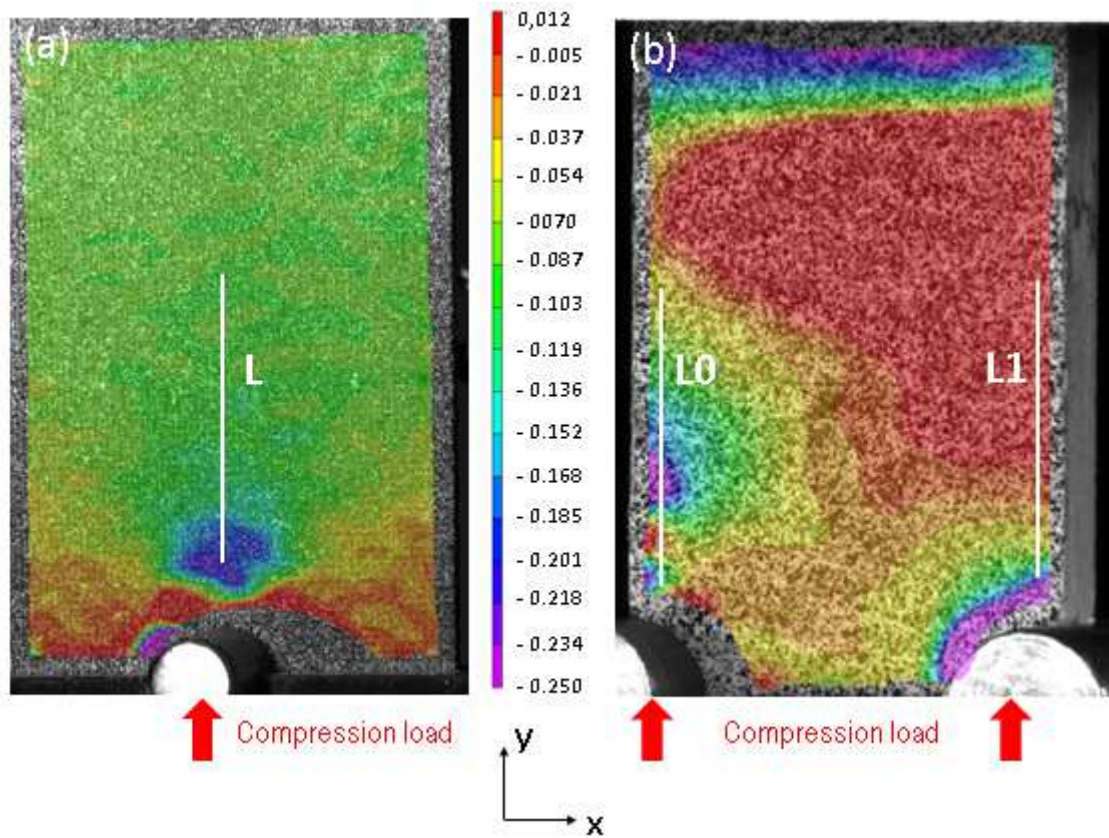


Figure 25: Longitudinal strain cartography (%) at the first bearing point: (a) standard bearing test, (b) BQH test

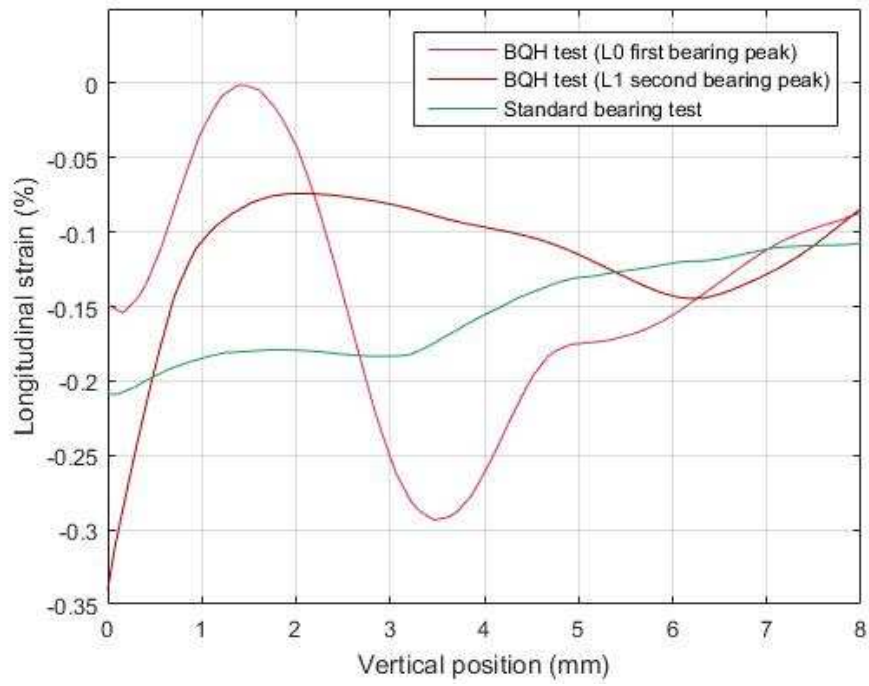


Figure 26: Longitudinal strain as a function of the vertical position

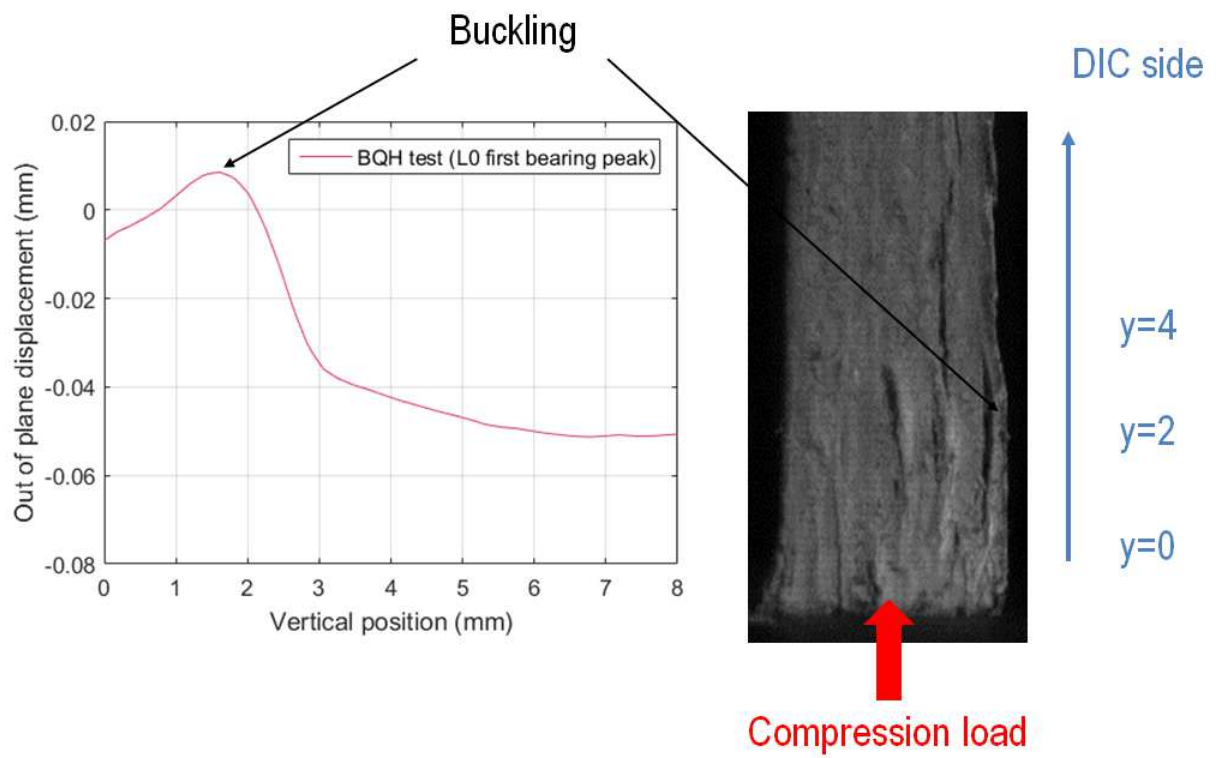


Figure 27 : Out of plane displacement at the first bearing peak (BQH₂₂, L0)

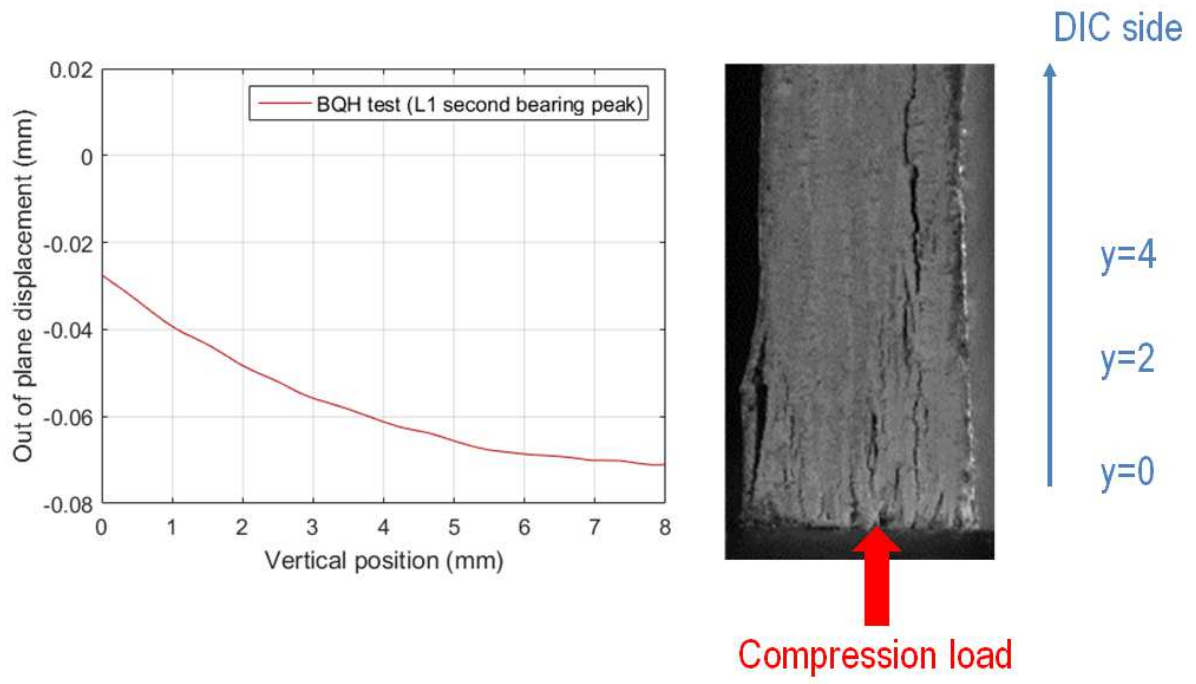


Figure 28 : Out of plane displacement at the second bearing peak (BQH22, L1)

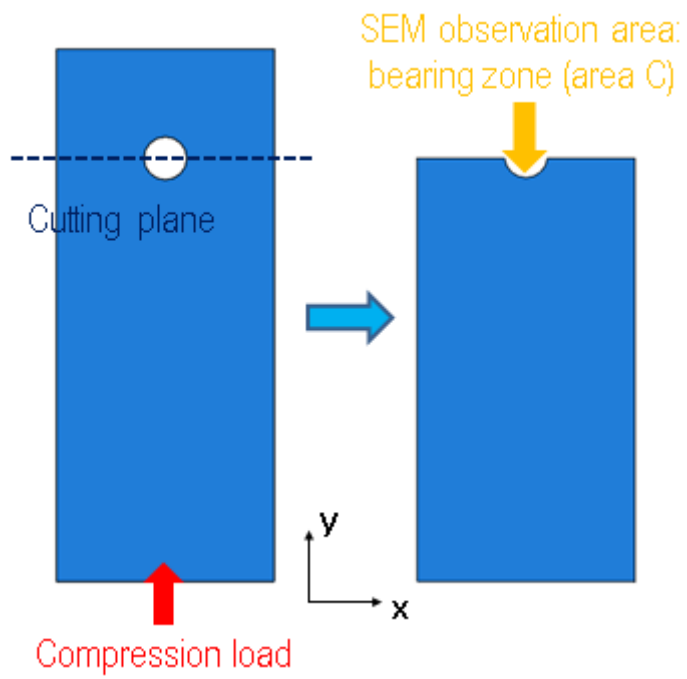


Figure 29: First SEM observation area (inside the hole)

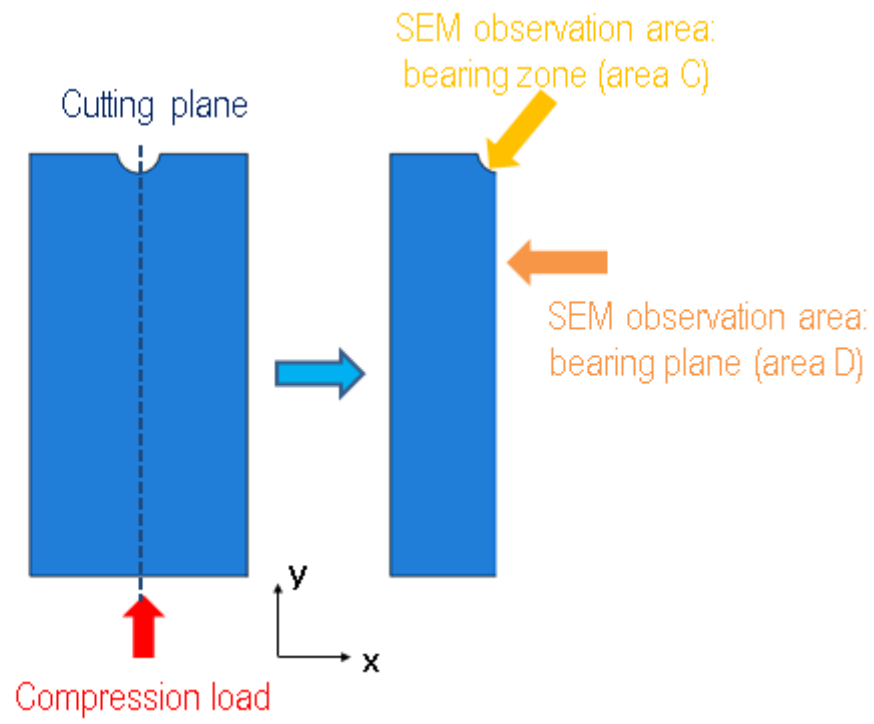


Figure 30: Second SEM observation area (on the bearing plane/bearing zone)

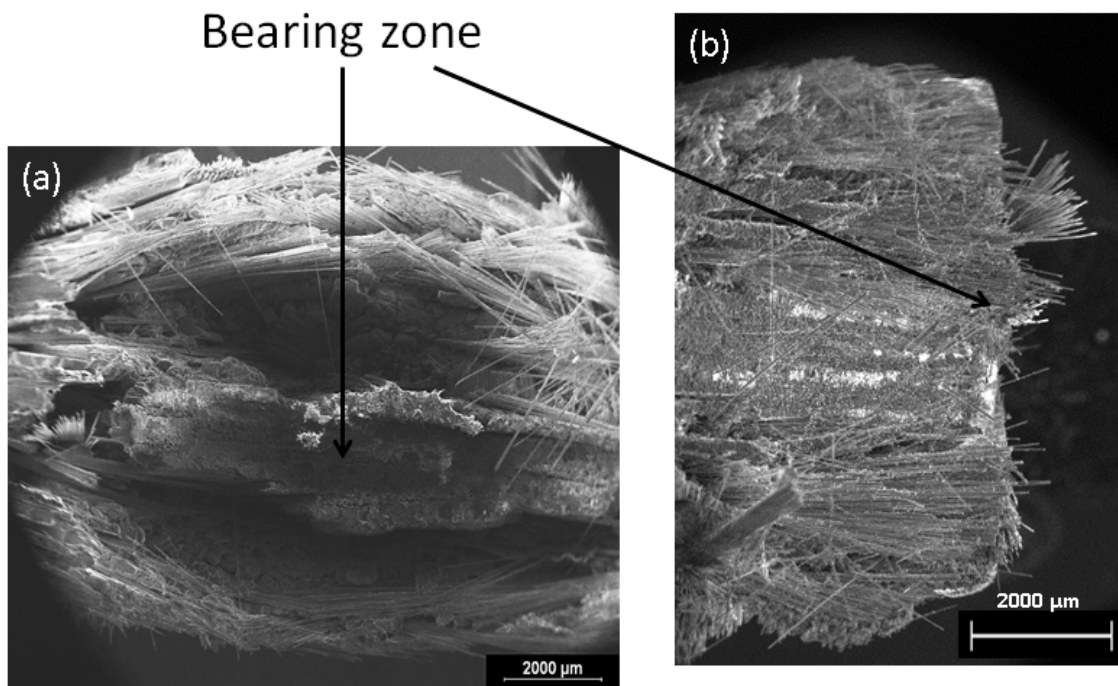


Figure 31: SEM images of the specimen after the tests, showing the external plies more damaged than the internal ones: (a) on a standard bearing test (area C) and (b) on a BQH test (area A)

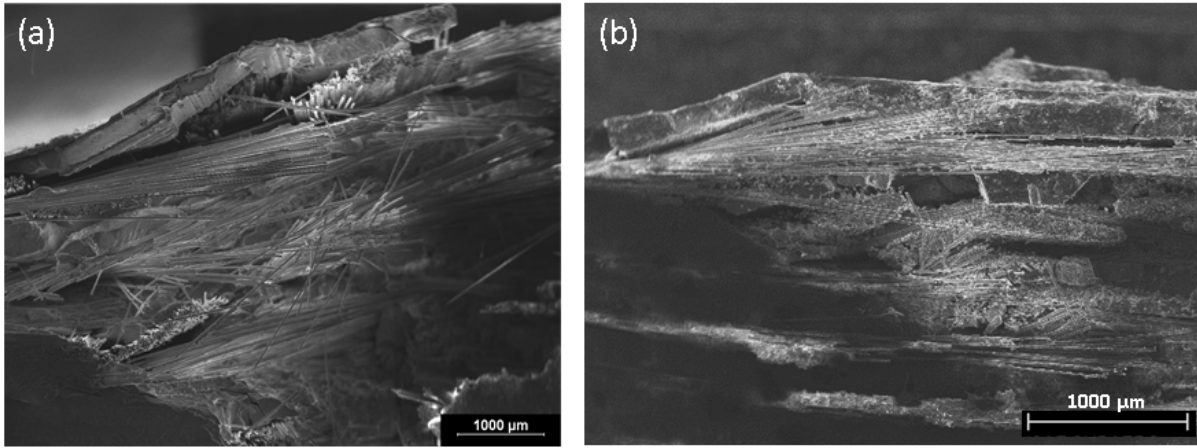


Figure 32: SEM images of the breakage of the external plies: (a) on a standard bearing test (area D) and (b) on a BQH test (area B)

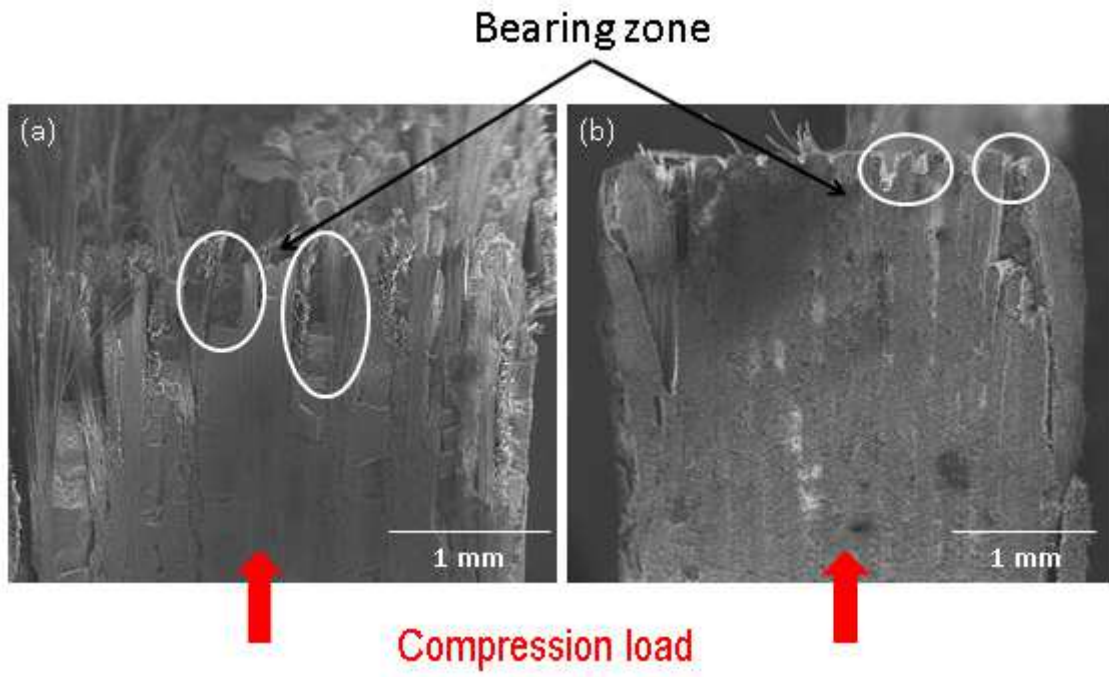


Figure 33: SEM images of tow breakage: (a) on a standard bearing test (area D) and (b) on a BQH test (area A)

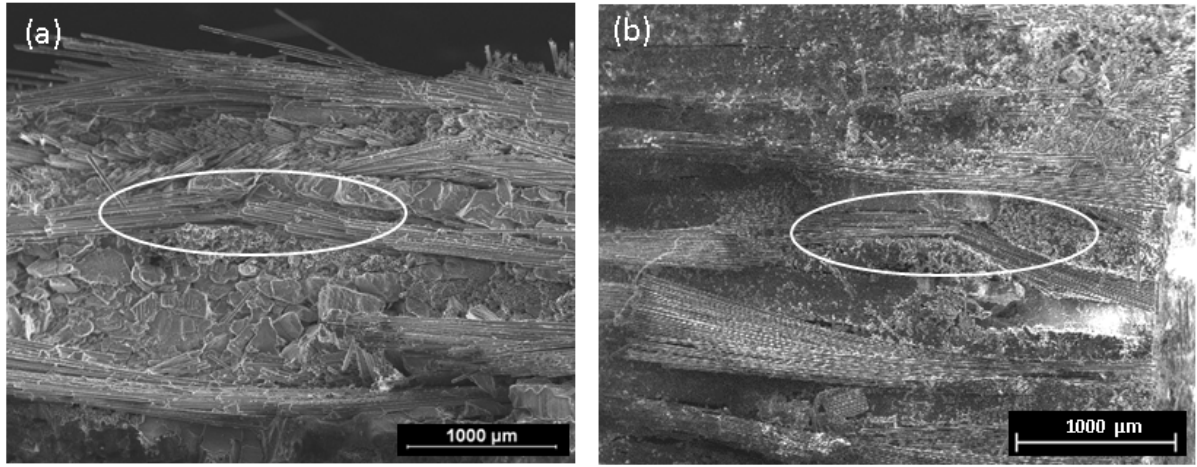


Figure 34: SEM images of kinking due to the bearing failure: (a) on a standard bearing test (area D) and (b) on a BQH test (area B)

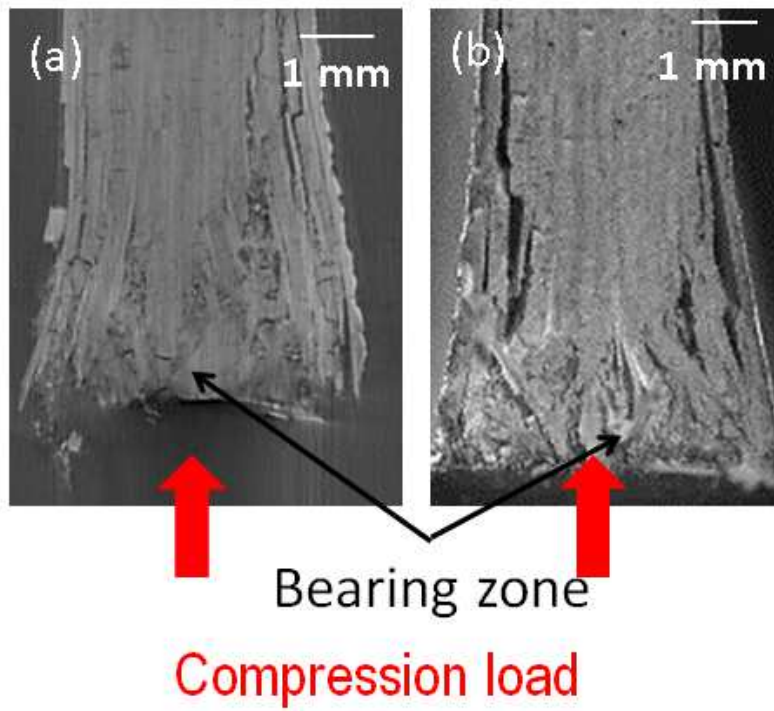


Figure 35: Damage after failure on the slice of the specimen: (a) tomography of the bearing plane on a standard bearing test and (b) high speed camera image on a BQH test

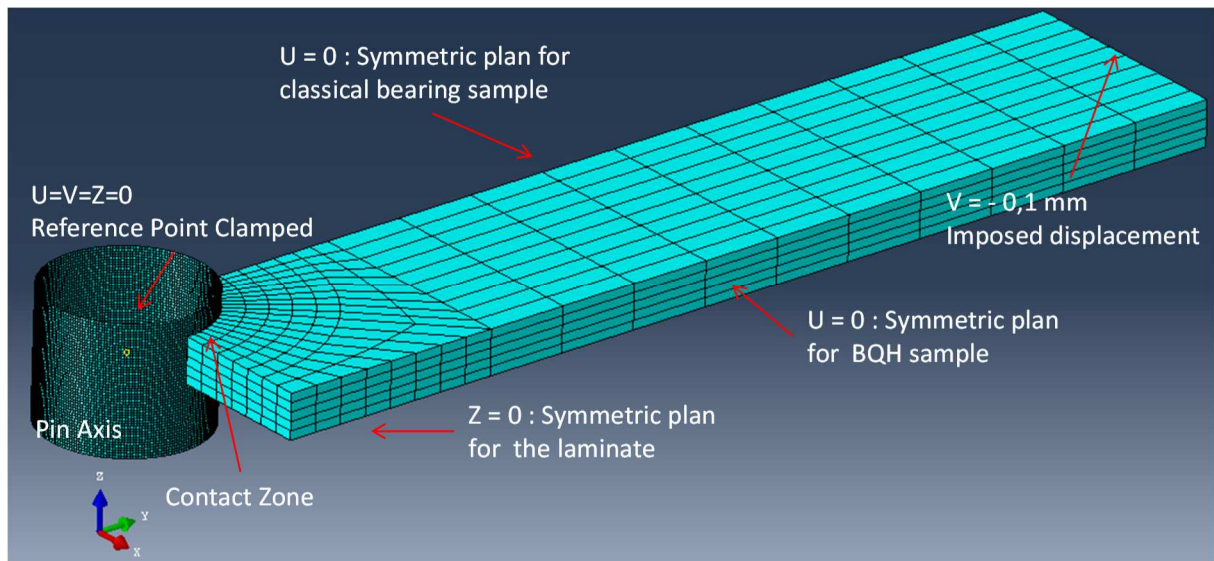


Figure 36: Finite Element model of the two test configurations: Mesh example for one brick element per ply.

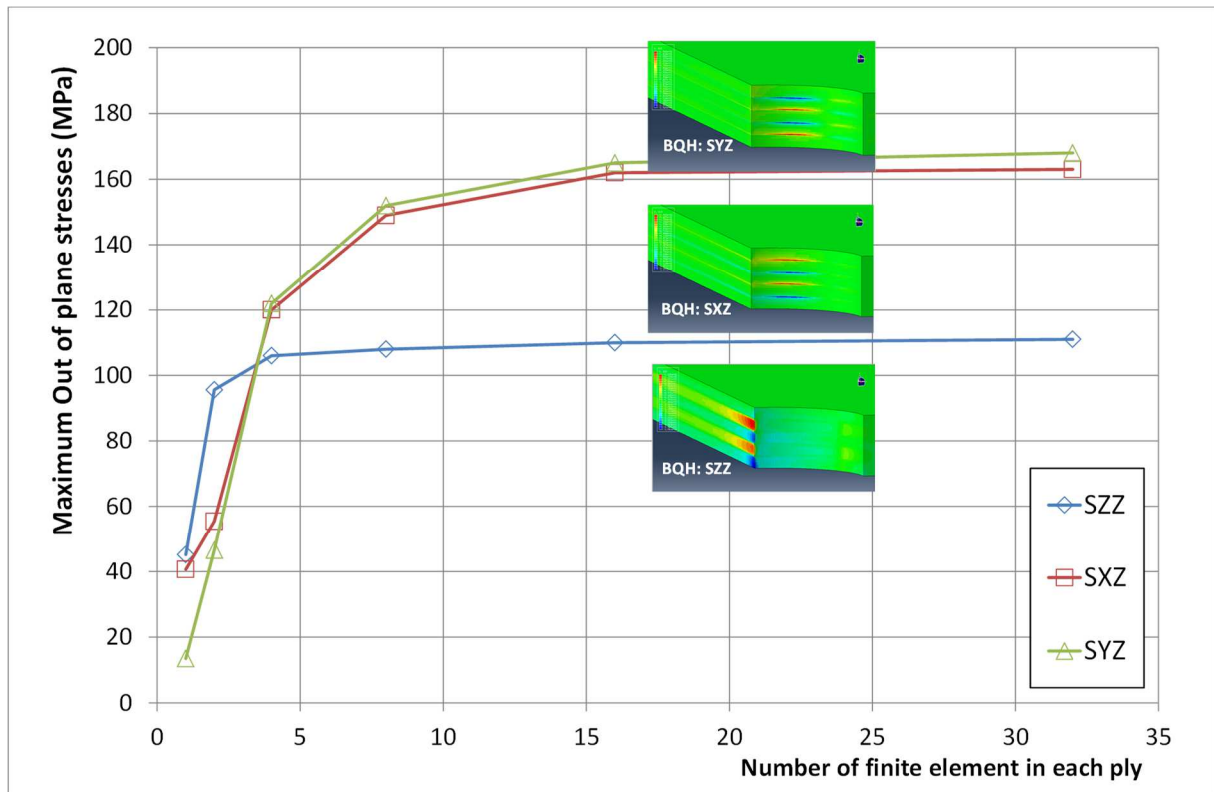


Figure 37: Mesh convergence study for BHQ FE model.

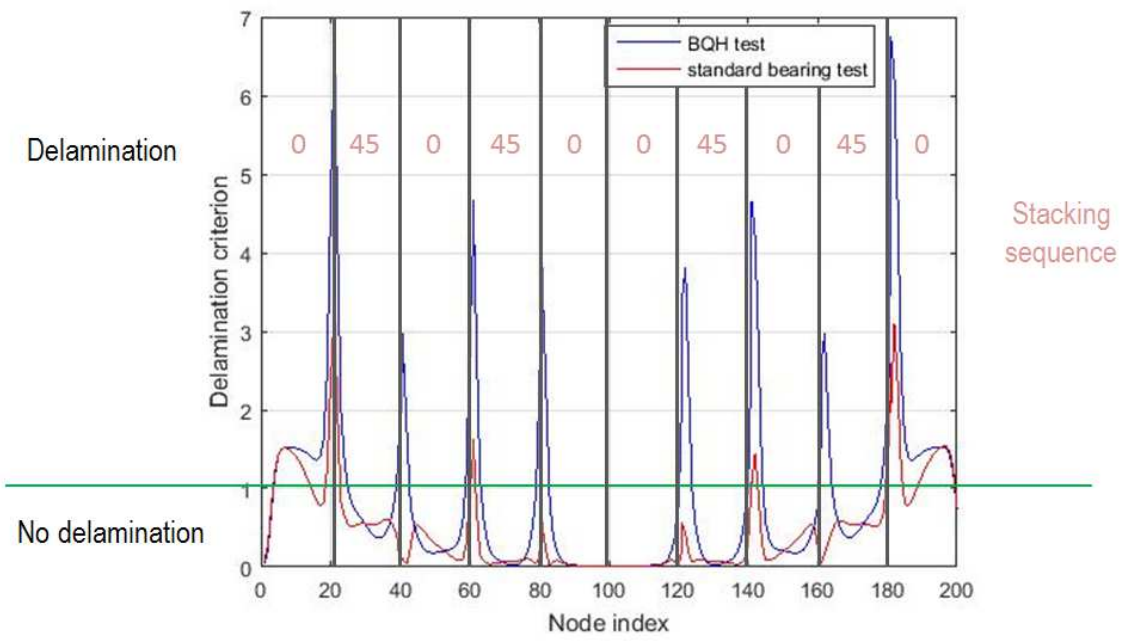


Figure 38: Delamination criterion of both configurations for [0/45/0/45/0]_s stacking sequence

s

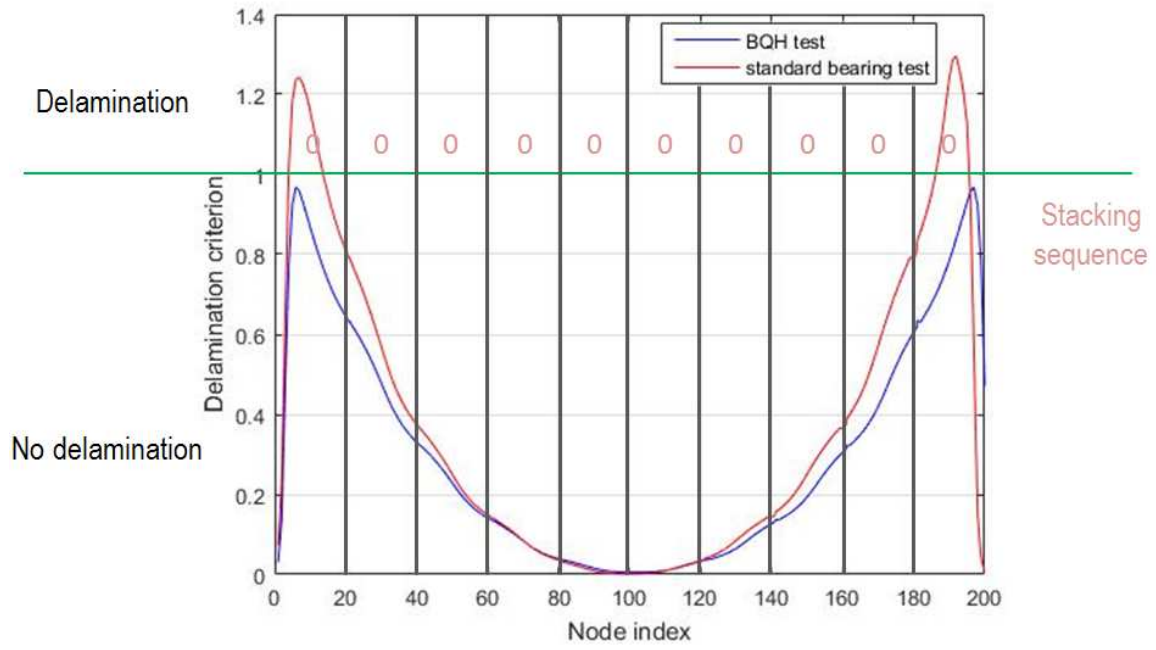


Figure 39: Delamination criterion of both configurations for $[0]_{10}$ stacking sequence